arXiv:1811.09565v1 [astro-ph.CO] 23 Nov 2018

FIRST COSMOLOGY RESULTS USING TYPE IA SUPERNOVAE FROM THE DARK ENERGY SURVEY: SURVEY OVERVIEW AND SUPERNOVA SPECTROSCOPY

C. B. D'Andrea[1], M. Smith[2], M. Sullivan[2], R. C. Nichol[3], R. C. Thomas[4], A. G. Kim[4], A. Möller[5,6], M. Sako[1], F. J. Castander[7,8], A. V. Filippenko[9,10], R. J. Foley[11], L. Galbany[12], S. González-Gaitán[13], E. Kasai[14,15], R. P. Kirshner[16,17], C. Lidman[6], D. Scolnic[18], D. Brout[1], T. M. Davis[19], R. R. Gupta[4], S. R. Hinton[19], R. Kessler[20,18], J. Lasker[20,18], E. Macaulay[3], R. C. Wolf[21], B. Zhang[5,6], J. Asorey[22], A. Avelino[23], B. A. Bassett[24,15,25,26], J. Calcino[19], D. Carollo[27], R. Casas[7,8], P. Challis[23], M. Childress[2], A. Clocchiatti[28], S. Crawford[15,29], K. Glazebrook[30], D. A. Goldstein[31], M. L. Graham[32], J. K. Hoormann[19], K. Kuehn[33], G. F. Lewis[34], K. S. Mandel[35], E. Morganson[36], D. Muthukrishna[5,37,6], P. Nugent[4], Y.-C. Pan[38,39], M. Pursiainen[2], R. Sharp[6], N. E. Sommer[5,6], E. Swann[3], B. E. Tucker[5,6], S. A. Uddin[40], P. Wiseman[2], W. Zheng[41], T. M. C. Abbott[42], J. Annis[43], S. Avila[3], K. Bechtol[44,45], G. M. Bernstein[1], E. Bertin[46,47], D. Brooks[48], D. L. Burke[49,50], A. Carnero Rosell[51,52], M. Carrasco Kind[53,36], J. Carretero[54], C. E. Cunha[49], L. N. da Costa[52,55], C. Davis[49], J. De Vicente[51], H. T. Diehl[43], T. F. Eifler[56,57], J. Estrada[43], J. Frieman[43,18], J. García-Bellido[58], E. Gaztanaga[7,8], D. W. Gerdes[59,60], D. Gruen[49,50], R. A. Gruendl[53,36], D. Gschwend[52,55], G. Gutierrez[43], W. G. Hartley[48,61], D. L. Hollowood[11], K. Honscheid[62,63], B. Hoyle[64,65], D. J. James[66], M. W. G. Johnson[36], M. D. Johnson[36], N. Kuropatkin[43], T. S. Li[43,18], M. Lima[67,52], M. A. G. Maia[52,55], J. L. Marshall[68], P. Martini[62,69], F. Menanteau[53,36], C. J. Miller[59,60], R. Miquel[70,54], E. Neilsen[43], R. L. C. Ogando[52,55], A. A. Plazas[57], A. K. Romer[71], E. Sanchez[51], V. Scarpine[43], M. Schubnell[60], S. Serrano[7,8], I. Sevilla-Noarbe[51], F. Sobreira[72,52], E. Suchyta[73], G. Tarle[60], D. L. Tucker[43], and W. Wester[43]

(DES Collaboration)

[1] Department of Physics and Astronomy, University of Pennsylvania, Philadelphia, PA 19104, USA
[2] School of Physics and Astronomy, University of Southampton, Southampton, SO17 1BJ, UK
[3] Institute of Cosmology and Gravitation, University of Portsmouth, Portsmouth, PO1 3FX, UK
[4] Lawrence Berkeley National Laboratory, 1 Cyclotron Road, Berkeley, CA 94720, USA
[5] ARC Centre of Excellence for All-sky Astrophysics (CAASTRO)
[6] The Research School of Astronomy and Astrophysics, Australian National University, ACT 2601, Australia
[7] Institut d'Estudis Espacials de Catalunya (IEEC), 08034 Barcelona, Spain
[8] Institute of Space Sciences (ICE, CSIC), Campus UAB, Carrer de Can Magrans, s/n, 08193 Barcelona, Spain
[9] Department of Astronomy, University of California, Berkeley, CA 94720-3411, USA
[10] Miller Senior Fellow, Miller Institute for Basic Research in Science, University of California, Berkeley, CA 94720, USA
[11] Santa Cruz Institute for Particle Physics, Santa Cruz, CA 95064, USA
[12] PITT PACC, Department of Physics and Astronomy, University of Pittsburgh, Pittsburgh, PA 15260, USA
[13] CENTRA, Instituto Superior Técnico, Universidade de Lisboa, Av. Rovisco Pais 1, 1049-001 Lisboa, Portugal
[14] Department of Physics, University of Namibia, 340 Mandume Ndemufayo Avenue, Pionierspark, Windhoek, Namibia
[15] South African Astronomical Observatory, P.O.Box 9, Observatory 7935, South Africa
[16] Harvard-Smithsonian Center for Astrophysics, 60 Garden St., Cambridge, MA 02138,USA
[17] Gordon and Betty Moore Foundation, 1661 Page Mill Road, Palo Alto, CA 94304,USA
[18] Kavli Institute for Cosmological Physics, University of Chicago, Chicago, IL 60637, USA
[19] School of Mathematics and Physics, University of Queensland, Brisbane, QLD 4072, Australia
[20] Department of Astronomy and Astrophysics, University of Chicago, Chicago, IL 60637, USA
[21] Graduate School of Education, Stanford University, 160, 450 Serra Mall, Stanford, CA 94305, USA
[22] Korea Astronomy and Space Science Institute, Yuseong-gu, Daejeon, 305-348, Korea
[23] Harvard-Smithsonian Center for Astrophysics, 60 Garden St., Cambridge, MA 02138, USA
[24] African Institute for Mathematical Sciences, 6 Melrose Road, Muizenberg, 7945, South Africa
[25] Department of Mathematics, University of Cape Town, 7700, South Africa
[26] South African Radio Astronomical Observatory, Cape Town, South Africa
[27] INAF, Astrophysical Observatory of Turin, I-10025 Pino Torinese, Italy
[28] Millennium Institute of Astrophysics and Department of Physics and Astronomy, Universidad Católica de Chile, Santiago, Chile
[29] Space Telescope Science Institute, 3700 San Martin Drive, Baltimore, MD 21218, USA
[30] Centre for Astrophysics & Supercomputing, Swinburne University of Technology, Victoria 3122, Australia
[31] California Institute of Technology, 1200 East California Blvd, MC 249-17, Pasadena, CA 91125, USA
[32] Department of Astronomy, University of Washington, Box 351580, U.W., Seattle, WA 98195, USA
[33] Australian Astronomical Optics, Macquarie University, North Ryde, NSW 2113, Australia
[34] Sydney Institute for Astronomy, School of Physics, A28, The University of Sydney, NSW 2006, Australia
[35] Institute of Astronomy and Kavli Institute for Cosmology, Madingley Road, Cambridge, CB3 0HA, UK
[36] National Center for Supercomputing Applications, 1205 West Clark St., Urbana, IL 61801, USA
[37] Institute of Astronomy, University of Cambridge, Madingley Road, Cambridge CB3 0HA, UK
[38] Division of Theoretical Astronomy, National Astronomical Observatory of Japan, 2-21-1 Osawa, Mitaka, Tokyo 181-8588, Japan
[39] Institute of Astronomy and Astrophysics, Academia Sinica, Taipei 10617, Taiwan
[40] Observatories of the Carnegie Institution for Science, 813 Santa Barbara St., Pasadena, CA 91101, USA
[41] Department of Astronomy,University of California, Berkeley, CA 94720-3411, USA
[42] Cerro Tololo Inter-American Observatory, National Optical Astronomy Observatory, Casilla 603, La Serena, Chile
[43] Fermi National Accelerator Laboratory, P. O. Box 500, Batavia, IL 60510, USA
[44] LSST, 933 North Cherry Avenue, Tucson, AZ 85721, USA
[45] Physics Department, 2320 Chamberlin Hall, University of Wisconsin-Madison, 1150 University Avenue Madison, WI 53706-1390
[46] CNRS, UMR 7095, Institut d'Astrophysique de Paris, F-75014, Paris, France
[47] Sorbonne Universités, UPMC Univ Paris 06, UMR 7095, Institut d'Astrophysique de Paris, F-75014, Paris, France
[48] Department of Physics & Astronomy, University College London, Gower Street, London, WC1E 6BT, UK
[49] Kavli Institute for Particle Astrophysics & Cosmology, P. O. Box 2450, Stanford University, Stanford, CA 94305, USA
[50] SLAC National Accelerator Laboratory, Menlo Park, CA 94025, USA

[51] Centro de Investigaciones Energéticas, Medioambientales y Tecnológicas (CIEMAT), Madrid, Spain
[52] Laboratório Interinstitucional de e-Astronomia - LIneA, Rua Gal. José Cristino 77, Rio de Janeiro, RJ - 20921-400, Brazil
[53] Department of Astronomy, University of Illinois at Urbana-Champaign, 1002 W. Green Street, Urbana, IL 61801, USA
[54] Institut de Física d'Altes Energies (IFAE), The Barcelona Institute of Science and Technology, Campus UAB, 08193 Bellaterra
(Barcelona) Spain
[55] Observatório Nacional, Rua Gal. José Cristino 77, Rio de Janeiro, RJ - 20921-400, Brazil
[56] Department of Astronomy/Steward Observatory, 933 North Cherry Avenue, Tucson, AZ 85721-0065, USA
[57] Jet Propulsion Laboratory, California Institute of Technology, 4800 Oak Grove Dr., Pasadena, CA 91109, USA
[58] Instituto de Fisica Teorica UAM/CSIC, Universidad Autonoma de Madrid, 28049 Madrid, Spain
[59] Department of Astronomy, University of Michigan, Ann Arbor, MI 48109, USA
[60] Department of Physics, University of Michigan, Ann Arbor, MI 48109, USA
[61] Department of Physics, ETH Zurich, Wolfgang-Pauli-Strasse 16, CH-8093 Zurich, Switzerland
[62] Center for Cosmology and Astro-Particle Physics, The Ohio State University, Columbus, OH 43210, USA
[63] Department of Physics, The Ohio State University, Columbus, OH 43210, USA
[64] Max Planck Institute for Extraterrestrial Physics, Giessenbachstrasse, 85748 Garching, Germany
[65] Universitäts-Sternwarte, Fakultät für Physik, Ludwig-Maximilians Universität München, Scheinerstr. 1, 81679 München, Germany
[66] Harvard-Smithsonian Center for Astrophysics, Cambridge, MA 02138, USA
[67] Departamento de Física Matemática, Instituto de Física, Universidade de São Paulo, CP 66318, São Paulo, SP, 05314-970, Brazil
[68] George P. and Cynthia Woods Mitchell Institute for Fundamental Physics and Astronomy, and Department of Physics and
Astronomy, Texas A&M University, College Station, TX 77843, USA
[69] Department of Astronomy, The Ohio State University, Columbus, OH 43210, USA
[70] Institució Catalana de Recerca i Estudis Avançats, E-08010 Barcelona, Spain
[71] Department of Physics and Astronomy, Pevensey Building, University of Sussex, Brighton, BN1 9QH, UK
[72] Instituto de Física Gleb Wataghin, Universidade Estadual de Campinas, 13083-859, Campinas, SP, Brazil
[73] Computer Science and Mathematics Division, Oak Ridge National Laboratory, Oak Ridge, TN 37831

Draft version November 26, 2018

ABSTRACT

We present spectroscopy from the first three seasons of the Dark Energy Survey Supernova Program (DES-SN). We describe the supernova spectroscopic program in full: strategy, observations, data reduction, and classification. We have spectroscopically confirmed 307 supernovae, including 251 type Ia supernovae (SNe Ia) over a redshift range of $0.017 < z < 0.85$. We determine the effective spectroscopic selection function for our sample, and use it to investigate the redshift-dependent bias on the distance moduli of SNe Ia we have classified. We also provide a full overview of the strategy, observations, and data products of DES-SN, which has discovered 12,015 likely supernovae during these first three seasons. The data presented here are used for the first cosmology analysis by DES-SN ('DES-SN3YR'), the results of which are given in DES Collaboration (2018a).

1. INTRODUCTION

Type Ia supernovae (SNe Ia) have fundamentally changed our understanding of the universe. It is through their utility as accurate distance indicators that the High-Z Supernova Search Team (Riess et al. 1998) and the Supernova Cosmology Project (Perlmutter et al. 1999) were able to make the groundbreaking discovery that the expansion of the universe is accelerating. To date, the nature of the substance causing this phenomenon, commonly referred to as 'dark energy,' remains unknown.

The quest for understanding the cause of the acceleration and constraining the models that describe it have motivated ever-improving supernova searches over the past two decades. At redshift $z \leq 1$ these cosmology-oriented programs include the Supernova Legacy Survey (SNLS; Astier et al. 2006; Sullivan et al. 2011; Conley et al. 2011), the Sloan Digital Sky Survey-II Supernova Program (SDSS-II; Frieman et al. 2008; Kessler et al. 2009a; Sako et al. 2008, 2018), ESSENCE (Wood-Vasey et al. 2007; Miknaitis et al. 2007; Narayan et al. 2016), and more recently, Pan-STARRS (Scolnic et al. 2014; Rest et al. 2014; Scolnic et al. 2018). The low-redshift sample necessary for anchoring the Hubble diagram includes Calán-Tololo (Hamuy et al. 1996), several CFA samples (Riess et al. 1999; Jha et al. 2006; Hicken et al. 2009, 2012), the Carnegie Supernova Project (CSP; Contreras et al. 2010), and, more recently, the homogeneous Foundation Survey (Foley et al. 2018). Nearly all observations

of SNe Ia at $z > 1.1$ are obtained from space, with only a few dozen well-observed objects to date (Riess et al. 2004, 2007; Suzuki et al. 2012; Riess et al. 2018).

The surveys described above all obtain distance measurements from light-curve fits to cadenced multi-color photometry (Phillips 1993; Riess et al. 1996; Tripp 1998). But to define the sample of SNe Ia used in a cosmological analysis requires a parallel spectroscopic follow-up program. This allows the survey to differentiate observed transients between SNe Ia and other classes of supernova, while also obtaining precise redshifts for the objects. Thus, the spectroscopic program determines what data are included in a Hubble diagram, as well as the position of these data along one axis.

For supernova surveys in the range of $0.1 < z < 1.0$, the spectroscopic program typically requires more observing time, and on larger telescopes, than does the entire photometric observing program—all of this to classify a small subset of detected transients. For example, SNLS used ~ 900 hours of spectroscopy on 8-10m class telescopes to spectroscopically classify 285 SNe Ia in the first three years of their survey (Howell et al. 2005; Bronder et al. 2008; Balland et al. 2009; Ellis et al. 2008), compared to 779 hours of good-quality photometry (Guy et al. 2010). Similarly large resources were dedicated by other large programs in this redshift range, such as ESSENCE (213 SNe Ia; Matheson et al. 2005; Foley et al. 2009; Narayan et al. 2016), Pan-STARRS1 (361 SNe Ia; Rest et al. 2014; Scolnic et al. 2018) and SDSS-II (500

SNe Ia; Zheng et al. 2008; Sako et al. 2018).

In this paper we describe the supernova spectroscopy program for the first three seasons of the Dark Energy Survey - Supernova Program (DES-SN), and give an overview of the survey and its operations. This is part of a series of companion papers supporting the first cosmological analysis of spectroscopically-classified SNe Ia from DES-SN ('DES-SN3YR'). These include detailed papers on aspects of SN search and discovery (Kessler et al. 2015; Goldstein et al. 2015; Morganson et al. 2018), our photometry pipeline (Brout et al. 2018b), photometric calibration (Burke et al. 2018; Lasker et al. 2018), simulations (Kessler et al. 2018), and a technique to account for simulation bias (Kessler & Scolnic 2017). Our analysis methodology and systematic uncertainties are presented by Brout et al. (2018a), and these results are used to constrain cosmology (DES Collaboration 2018a) and the Hubble constant (Macaulay et al. 2018). The DES-SN3YR constraints are combined with other DES probes in DES Collaboration (2018b). A new Bayesian Hierarchical Model for supernova cosmology is tested by Hinton et al. (2018).

The format of the paper is as follows. In Section 2 we describe the strategy and status of the overall DES-SN observing program. In Section 3 we describe how SN candidates are defined and extracted from the data, while Section 4 details the spectroscopic follow-up campaign for each observatory used in our program. In Section 5 we derive the effective spectroscopic selection function from the classifications obtained by our program, essential for understanding the biases in a spectroscopically derived SN Hubble diagram from DES. We conclude in Section 6 by looking toward future releases and analyses of DES data.

2. THE DES SUPERNOVA PROGRAM
2.1. *Dark Energy Survey*

The Dark Energy Survey (DES Collaboration 2016) is a 6 year, ~ 570 night survey using the 4-meter Blanco telescope at Cerro-Tololo Inter-American Observatory (CTIO) in Chile. It uses the Dark Energy Camera (DECam; Flaugher et al. 2015), a 520 megapixel wide-field imager with a $2.2°$ field of view and deep-depleted CCDs, giving it excellent quantum efficiency out to 1 micron. Commissioning of the camera began in September 2012, and a period of data-taking by DES called Science Verification ('SV') was carried out from November 2012 through February 2013. The first season of the survey ('Y1') began on August 31, 2013, and the third season ('Y3') ended February 12, 2016.

DES is designed as a Stage 3 dark-energy experiment according to the Dark Energy Task Force (DETF) Figure of Merit (Albrecht et al. 2006), increasing the constraints on the w_0-w_a plane by a factor of a few. It combines four probes of dark energy – weak lensing, large-scale structure, galaxy clusters, and SNe Ia – into one experiment sharing a common instrument, allowing for consistent calibration, validation, and a better understanding of systematic errors in the combined analysis. DES is split into two distinct observing modes: the wide-area survey (DES-wide), observing 5000 square degrees in $grizY$ to a 5σ depth of ~ 23.5; and DES-SN.

The observing strategy for DES-SN is optimized for the purposes of SN Ia cosmology. With this in mind, different observing strategies were explored by Bernstein et al. (2012). The selected and implemented strategy for DES-SN is a 10-field hybrid-depth survey, designed to obtain a few thousand well-observed light curves of SNe Ia over a redshift range $0.2 < z < 1.2$.

There are three defining aspects of DES-SN. The first is the excellent z-band response of DECam owing to the deep-depleted CCDs (Diehl et al. 2014). This allows for rest-frame optical light curves of $z \approx 1$ SNe Ia to be well-measured. The second is excellent calibration, as this is the largest systematic uncertainty in SN Ia cosmology (Scolnic et al. 2018). The DES Science Requirements state that the survey must be calibrated to 0.5% in its absolute calibrations and colors.

The third defining aspect is photometric classification of SNe Ia. The field-of-view of DECam is much larger than that of any previous camera on a similarly sized telescope, allowing DES-SN to observe an unprecedented area for its depth. Thus, given the quantity of faint SNe that DES-SN discovers, any realistic spectroscopic resource allocation will only permit spectroscopic classification for a small fraction of these SNe. To make optimal use of the DES-SN data we therefore will rely on photometric classification for our primary cosmology analysis. This does not remove the need for spectroscopic follow-up observations of live SNe, but rather places different priorities on the follow-up program, as explained in Section 4.

In the remainder of this section we first describe in detail the first three seasons of the DES-SN observing program.

2.2. *Exposure Time and Depth*

For a fixed amount of observing time there is a direct trade-off between depth and area. Based on simulations of different survey strategies (Bernstein et al. 2012), DES-SN has been designed to have fields of two different depths: eight 'shallow' and two 'deep' fields, where each field is a single pointing of DECam. The deep fields serve to extend the redshift range of cosmologically useful SNe Ia out to $z \approx 1.2$, while the more numerous shallow fields add volume and numbers at intermediate redshifts. The total exposure time for each filter and the median limiting magnitude for both the deep and shallow fields are given in Table 1. Unlike DES-wide, DES-SN observes in only $griz$, as Y-band exposures provide too little additional information to justify the significant added cost in exposure time. Longer observations are split into a number of shorter exposures and coadded (e.g., 11 exposures for the 1hr per-epoch z-band deep fields). We note that the limiting magnitude is derived from artificially inserting supernovae into our processing pipeline and determining the magnitude at which 50% of all such objects are recovered (Kessler et al. 2015). As such, these limits take into account real observing conditions and template noise, and are 0.5 to 1 mag shallower than when computed with the DECam Exposure Time Calculator (ETC)[1], as was also discussed by Förster et al. (2016). Throughout the text, we refer to an observation of one field, in one filter, on one night, as a 'filter-epoch'.

Table 1
Exposure Times

Filter	Shallow Field			Deep Field		
	t_{exp}[a]	N_{exp}[b]	Depth[c]	t_{exp}[a]	N_{exp}[b]	Depth[c]
g	175	1	23.7	600	3	24.6
r	150	1	23.6	1200	3	24.8
i	200	1	23.5	1800	5	24.7
z	400	2	23.3	3630	11	24.4

[a] Total exposure time per filter-epoch (in seconds).
[b] Number of exposures per filter-epoch.
[c] Median limiting magnitude per pointing over the first 3 seasons of DES-SN, defined as the magnitude at which 50% of fake supernovae inserted into pipeline are recovered by difference imaging (Kessler et al. 2015).

Table 2
Field Locations

Legacy Field	DES Field	RA (J2000)	DEC
CDFS	C1	03h 37m 05.83s	-27:06:41.8
	C2	03h 37m 05.83s	-29:05:18.2
	C3	03h 30m 35.62s	-28:06:00.0
Elais-S1	E1	00h 31m 29.86s	-43:00:34.6
	E2	00h 38m 00.00s	-43:59:52.8
SDSS Stripe 82	S1	02h 51m 16.80s	00:00:00.0
	S2	02h 44m 46.66s	-00:59:18.2
XMM-LSS	X1	02h 17m 54.17s	-04:55:46.2
	X2	02h 22m 39.48s	-06:24:43.6
	X3	02h 25m 48.00s	-04:36:00.0

DECam has a 2.2° diameter field-of-view and an observable area (excluding chip gaps) of 2.7 deg². This gives the DES-SN program a total observing area of 27 deg², nearly 7 times the area of SNLS. DES-SN does not dither over the gaps, since filling these in decreases the area repeatedly observed on the subsequent epoch. Dithers of order of a few arcseconds are carried out, allowing instrumental artifacts to be corrected in processing. Since dithers do not cross the chip gap, any object in a field appears on only one chip; therefore, our processing pipeline treats each chip independently.

2.3. Field Locations

The ten DES-SN fields are grouped in four distinct regions of the sky, coinciding with well-known legacy fields. Each region contains two adjacent shallow fields, and in two of the four regions there is also an adjacent deep field.

The prefix for each DES field name is derived from the name of the legacy field in which it is located: 'X' for the fields lying in the XMM-LSS footprint, 'C' for the fields clustered around the Chandra Deep Field - South (CDFS), 'E' for the fields in and around Elais-S1, and 'S' for fields located in SDSS - Stripe 82. The centroids of each field are given in Table 2. Shallow fields have a suffix of 1 or 2, with the more northerly field given the designation 1. Deep fields have a suffix of 3. All fields in the same region contain a small (order 1%) amount of overlap with one another.

The DES-SN fields lie within the DES-wide footprint to benefit from a consistent photometric calibration (Figure 1). This constraint forces all fields to be relatively close in RA, spanning only three hours. The fields are broadly distributed in declination in order to allow for
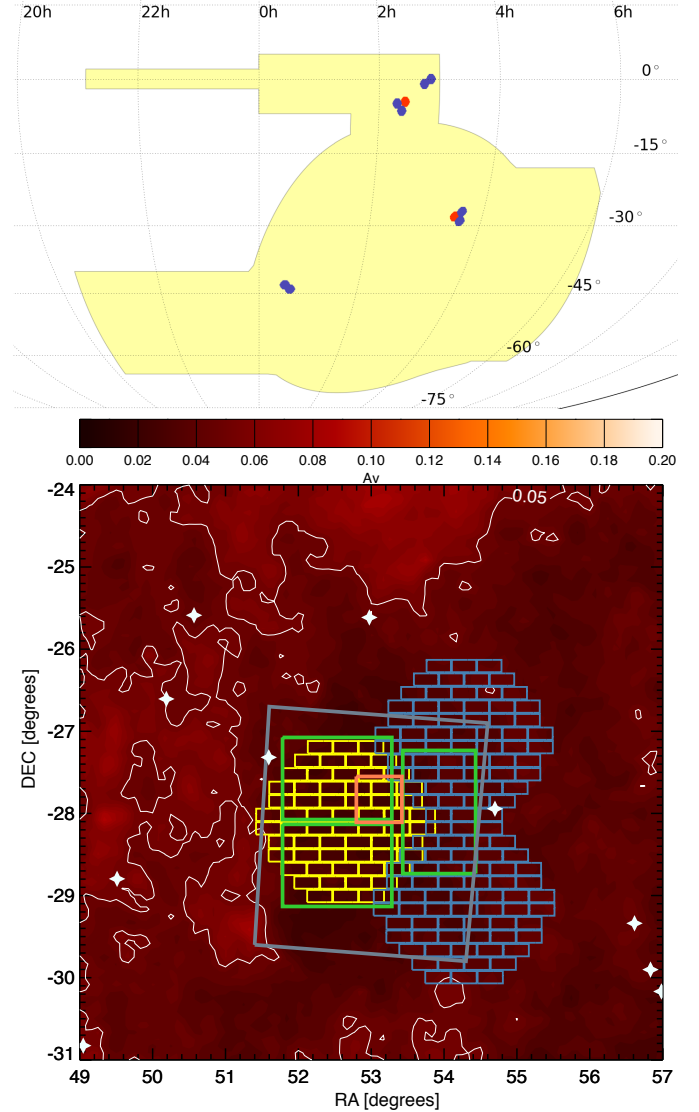

Figure 1. Top: The DES footprint (yellow), with the DES-SN shallow (blue) and deep (red) fields overplotted. A Mollweide equal-area projection is used. Positions of fields are listed in Table 2. **Bottom:** Enlarged view of the DES-SN C fields. The shallow fields (C1 and C2) are again in blue, and deep C3 is outlined in yellow. These DECam footprints are plotted over a contour plot of MW extinction. Bright stars ($M_V < 8$ mag) are plotted in white. Overplotted are the boundaries of fields observed by SWIRE (grey), VIDEO (green), and CDFS (orange).

spectroscopic follow-up observations at low airmass from northern observatories for half of the fields (X and S), while the C and E fields are more southerly to allow for longer windows at low airmass and better avoidance of the Moon.

In addition to considerations of calibration and spectroscopic follow-up, the DES-SN fields were located with Milky Way extinction and ancillary data in mind. Low-extinction regions were preferentially selected ($E(B - V) < 0.02$ mag in 8 of 10 fields), and overlap with other surveys was optimized. Particular attention was paid to overlap with deep near-infrared (VIDEO; Jarvis et al. 2013) and mid-infrared (SWIRE; Lonsdale et al. 2003) survey regions. Finally, field centroids were adjusted to minimize the area lost from masking of bright stars and

their bleed trails.

2.4. *Observing Strategy*

DES observes in 5-6 month seasons, starting in mid-late August and ending in early-mid February. The season is constrained from being extended by the requirement of low-airmass observations in the compact DES-wide footprint. The first and last month of each season are primarily scheduled as half-nights to ensure footprint visibility. The length of the continuous observing season helps to minimize edge effects for DES-SN light curves, particularly for highly time-dilated SNe at $z \geq 1$. Most DES nights are dark, but CTIO schedules grey and bright time for DES as well to provide the community time with DECam at a range of RA and sky brightness conditions. As such, the structure of DES-SN observations—survey duration, cadence, sky brightness—are the result of these competing interests.

DES uses an algorithmic scheduler (`ObsTac`; Neilsen & Annis 2014) to determine the survey program (DES-SN or DES-wide), field, and filter to observe given the present observing conditions, the completeness of the DES-wide footprint, and the length of time Δt_{seq} since the last accepted observation of each DES-SN sequence. A 'sequence' is defined as a series of exposures that are not interrupted once they begin, regardless of changing conditions. The number of exposures per filter, per field is listed in Table 1. For each of the DES-SN shallow fields a sequence is all of the exposures in all of the filters (*grizz*), while each filter-epoch is treated as a distinct sequence in each DES-SN deep field (*ggg,rrr,iiiii,zzzzzzzzzz*). This uncoupling of the long deep-field filter-epochs introduces scheduling flexibility for `ObsTac` to better optimize observations.

A DES-SN sequence is triggered if $\Delta t_{\mathrm{seq}} \geq 4$d and the seeing (measured at zenith in the i-band) is $\geq 1.1''$, or with no lower limit on the seeing if $\Delta t_{\mathrm{seq}} \geq 7$d. Priority is always given to the sequence with the largest Δt_{seq}. There are also upper limits on the projected seeing for the deep ($1.3''$) and shallow ($1.8''$) fields to minimize poor-quality data. DES-SN observations require the predicted sky brightness for a filter-epoch (in mag/arcsec^2 above dark) to be less than $3/3/2/2$ for $g/r/i/z$. For the shallow fields this is loosened to $5/4/2/2$ if $\Delta t_{\mathrm{seq}} \geq 7$d, as otherwise the filters being tied together in one observing sequence would result in long gaps *in red filters* due to the brightness of the moon. `ObsTac` additionally requires a starting airmass < 1.5 per sequence, though this is loosened at the edges of each season.

The data quality (DQ) for each exposure is assessed based on an analysis of its output from the difference imaging pipeline (`DiffImg`; Kessler et al. 2015). There are three possibilities for the status of an exposure: Pass, Fail, or Junk. Pass means minimal acceptable DQ has been achieved, and Fail means it has not. Specifically, an image fails DQ if the measured point-spread function (PSF), converted to i-band zenith, is $> 2.0''$, or if the artificial sources of magnitude 20 we insert into our pipeline have a measured signal-to-noise ratio (SNR) of < 20 (< 80 for the deep fields). Junk means that the pipeline was unable to process the image, either due to instrumental errors or exceedingly poor weather. If an exposure is labeled as Fail or Junk, then it is not considered 'accepted', and the clock for re-taking the sequence (Δt_{seq}) is not reset to zero.

2.5. *Survey Summary*

The DES-SN program took 6,877 exposures totaling 487.69 hours of on-sky time during the first three years of the survey. Data quality was assessed as Pass for 87.7 percent of the exposure time. The mean number of total (Pass) epochs per field, per season was 29.3 (24.6) for each shallow field and 25.6 (22.7) for each deep field. The number of good filter-epochs per season varied from 15-28, while the total number ranged from 21-32.

The mean duration of the observing season for each DES-SN field was 167 days, with only small variations across the seasons (163/168/170). The observing season per field varied from 153 days (X3r in Y3) to 182 days (C3z in Y2). Typically the southern fields have a longer continuous visibility than the more northerly fields (171 days for SN-C and SN-E; 160 and 164 for SN-S and SN-X, respectively.)

The mean cadence for DES was 7.4d when considering only good-quality imaging; the cadence was 6.1d when including all imaging. The shallow fields have a slightly better cadence than the deep fields (7.3d and 7.8d, respectively). The shallow fields vary between a cadence of 7.1d to 7.5d, and in the deep fields – where bands are observed independently – there is no effective difference in cadence (range of 7.7d to 7.9d). The median for all of the above quantities is 7d.

We show the full observing history of the first three years of DES-SN in Figure 2, and condense this information into a histogram in Figure 3. 68% of all epochs were taken with a cadence of 4-8 days, and 23% were taken with a cadence of 9-13 days. Although observations are given top priority programatically at $\Delta t_{\mathrm{seq}} = 7$d, a number of factors cause a long tail to higher cadences. In particular, there are poor weather nights, nights DES is off-sky for community time, nights when sky brightness is above the observing threshold, and nights when the time allotted for programmed DES-SN sequences exceeds the time of field visibility.

We note that there are cases where we have a cadence < 4 days, seemingly in contradiction with `ObsTac`. There are two causes for this. The majority of the short-cadence exposures (79%) come from a shallow-field sequence where one filter fails DQ but the others pass; in these cases Δt_{seq} is not reset, which can lead to short cadences for some filters. The remaining short-cadence exposures are due to data-processing lags, where DQ was not accessed prior to the next night's observations.

We have only 61 filter-epochs with a gap in the cadence > 15 days, on average 0.5 per filter-epoch per season. Fewer than half of these gaps occur between September 15 and January 31. Therefore, most of the large light-curve gaps are at the very beginning (when weather is often poor), or at the very end of the season, when overriding of `ObsTac` was permitted. As the end of the DES-SN season is for completing already discovered SN light curves rather than searching for new SNe, assessment of overall DES collaboration needs permitted a reduced DES-SN cadence without sacrificing SNe that could potentially be part of a cosmological-analysis sample.

In Figure 4 we show the cumulative distribution function (CDF) for the measured full-width at half-
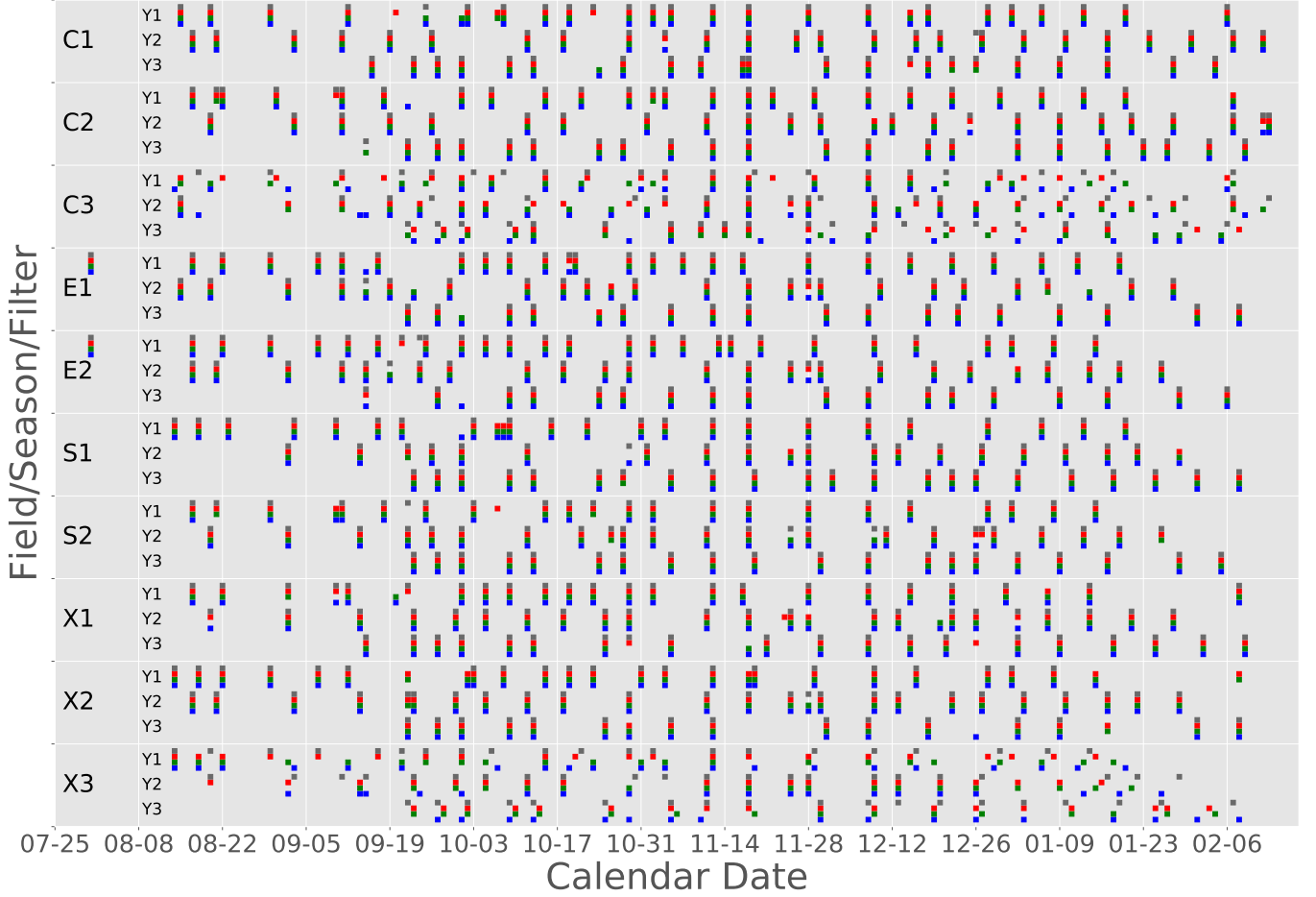
Figure 2. Every accepted observation taken over the first three seasons of DES-SN, with $g/r/i/z$ denoted as blue/green/red/grey. Each of the 10 fields is grouped together and data are shown for all three seasons. In the deep fields individual filters can be observed on different nights, whereas the shallow fields are grouped together as one observing block.
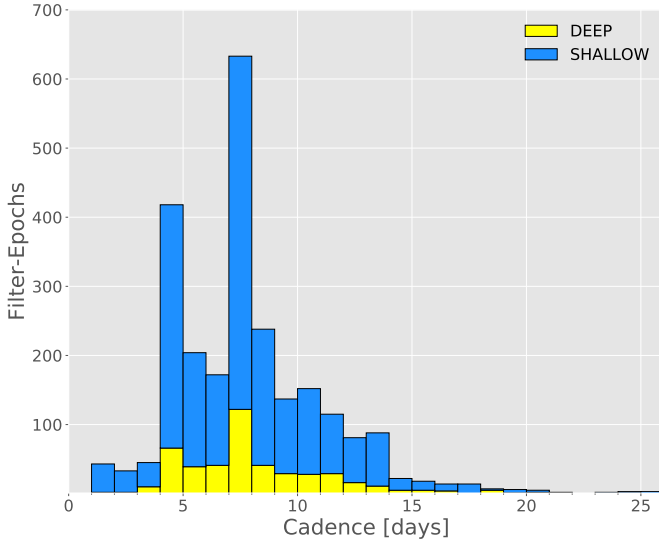

Figure 3. Stacked histogram of the number of days between good-quality data in a single filter-epoch over the first three years of the DES-SN program, split between deep (yellow) and shallow (blue) fields. Note the peak at 4 days (when observations can be made owing to adequate seeing), and at 7 days (when observations begin to be forced regardless of the seeing).

maximum intensity (FWHM) of the PSF for each DES-SN exposure, split by band and depth. The measured FWHM is worse for bluer bands, as the atmosphere produces a larger PSF for smaller wavelengths. The median observed FWHM in $griz$ (in arcseconds) is $1.41/1.29/1.17/1.09$. We note that ObsTac does not use this measurement but rather the i-band zenith PSF to schedule observations, and as expected from our observing algorithm, the median of this statistic is consistent amongst all bands. We also note that the distributions in Figure 4 are similar between deep and shallow fields, with the exception that the poorest $\sim 10\%$ of images in the deep field were taken in significantly better conditions than those in the shallow fields, which is also to be expected from our observing algorithm.

In Figure 5 we plot the limiting magnitude of each filter-epoch, split by band. The median depth across all bands is very similar, which was the intended outcome of our chosen exposure times. We note that despite our usage of the term 'shallow', these fields have per-exposure depths of ~ 23.5 mag, deeper than SDSS and equal to or slightly deeper than Pan-STARRS Medium-Deep Survey (Sako et al. 2018; Rest et al. 2014). The larger variation in bluer bands is an effect of observing across a large variety of sky brightness conditions.
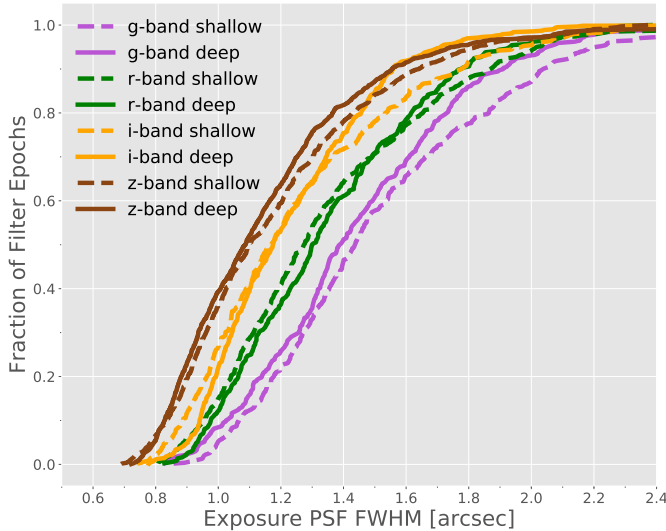
3. TRANSIENT IDENTIFICATION

Figure 4. Distribution of observed PSF FWHM (in arcseconds) for each exposure in the first three years of the DES-SN survey.

DES-SN data are processed nightly to find new transient candidates and to update the photometry for previously identified candidates. All data processing for DES takes place at the National Center for Supercomputing Applications (NCSA[2]) in Urbana-Champaign, Illinois. Here we briefly describe these steps and how they have evolved during the survey. We end this section with statistics for detections over the first three seasons of DES-SN.

3.1. *Image Processing & Difference Imaging Pipeline*

DES Observations are transferred from CTIO to NCSA within minutes of the end of each exposure, where they are preprocessed by the DES Data Management team (DESDM). This step includes bias subtraction, flat fielding, bad-pixel masking, and corrections for crosstalk and nonlinear pixel response. Next the images are run through the Supernova Single Epoch (SNSE) pipeline, where saturated stars and their bleed trails, cosmic rays, and satellites are masked out, and the sky is measured and subtracted from the image. Full details of preprocessing and SNSE pipelines can be found in Morganson et al. (2018).

Transients are identified from these images via the DES-SN Difference Imaging Pipeline `DiffImg`, described in detail by Kessler et al. (2015). Much of `DiffImg` makes use of publicly available codes or modifications thereof. All exposures in a given filter-epoch are coadded to form a single 'search image'. Template images for a given season are created by coadding images taken in good conditions during previous DES observing seasons (during Y1, images from SV were used as templates). Source extraction from both template and search images allows for a common astrometric solution to be determined. The images are PSF-matched, the template is subtracted from the search image, and sources are extracted from the resulting 'difference image'. Every source detected by `DiffImg` on every filter-epoch is classified as an 'object', and is saved in a database. These steps are run on each CCD individually.
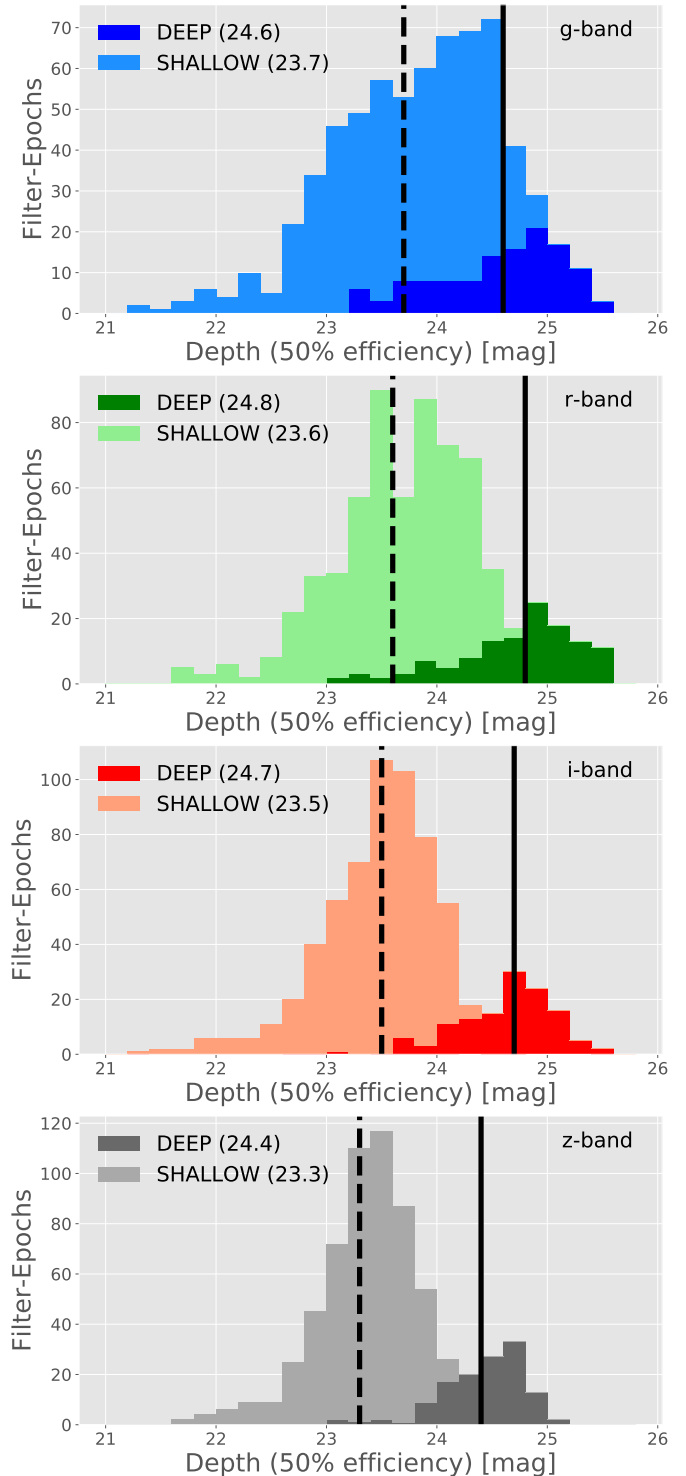
Figure 5. Depth of the DES filter-epochs in the first three seasons of the survey, split by deep and shallow fields. Median depth in the deep and shallow fields are shown by solid and dashed lines, respectively.

3.2. *autoScan*

We subsequently evaluate each object to determine whether it is a real astronomical point source or an artifact of the reduction pipeline (unmasked artifact, subtraction error, etc.). For this we developed a supervised machine-learning algorithm (`autoScan`; Goldstein et al.

2015) that assigns a score (0-1) to each object, where a higher score indicates a higher likelihood of the object being a non-artifact. The score is a function of many features computed directly from the images, most of which are ways to quantify the shape, size, and pixel-level flux distribution within the object. Goldstein et al. (2015) determine that the `autoScan` score should be ≥ 0.5 to optimize the detection efficiency with a minimal false detection rate. An object with an `autoScan` score ≥ 0.5 is labeled an 'ml_object' to specify that it has passed machine learning and is most likely a detection of a real astrophysical transient.

3.3. *Candidates and Transients*

The presence of multiple spatially and temporally coincident 'objects' triggers the creation of a 'candidate'. This is the most basic level in DES-SN of defining a likely astrophysical transient. We define spatially coincident as objects detected in different images within $1''$ of the same position, both of which have an `autoScan` score ≥ 0.3, in any combination of filters and detected less than 30 days apart. We note the loose `autoScan` threshold is intended to minimize the number of real transients that are discarded at this stage. All candidates receive a unique SuperNova IDentification number, or SNID. PSF-fitted photometry (i.e., 'forced photometry') is measured on all previous images at the candidate's position and updated with each subsequent observation (Kessler et al. 2015).

We define a 'transient' (hereafter *transient*) as a candidate consisting of at least two ml_objects and detected on more than one night. This higher threshold simultaneously removes slow-moving asteroids (which may be spatially coincident over one night) and lowers the contamination rate, a necessity for spectroscopic follow-up. We run our host-matching algorithm (Section 3.4) and do real-time light-curve fitting (Section 3.5) on all *transients*.

All *transients* receive unique names of the format 'DESXXYYzzzz' based on their location and the time of their discovery. For a *transient* discovered in a given observing season, 'XX' represents the last two digits of the year in which that observing season began: 13, 14, and 15 for DES Y1, Y2, and Y3, respectively. The DES-SN field the *transient* was first discovered in is given by 'YY', and 'zzzz' is a unique alphabetical identifier within the season that ascends as the season progresses (a, ..., z, aa, ..., zz, etc.). Owing to multiple reprocessings of data as incremental improvements were made to `DiffImg`, the naming system is no longer strictly sequential, and some irregularities – such as names no longer associated with a *transient* – occur. However, in no circumstance was a name ever used for two different candidates.

Finally, we developed a 'transient_status' flag to further improve the efficiency of our spectroscopic follow-up. This empirically derived flag removes the most commonly found cases of artifacts that pass our simple *transient* criteria. There are four indicators of an artifact we evaluate for: (i) pixel correlation (repeated detections on a single pixel, column, or row); (ii) band multiplicity (non-physical fraction of all detections occurring in single band); (iii) large temporal separation between detections (Δt between ml_objects); and (iv) large quantity of poor subtractions (indicating multiple good ml_objects by chance). These criteria are evaluated for each *tran-sient* separately over each DES season; a *transient* passing all criteria is given a positive flag. If a transient has a positive flag for multiple seasons, the flags are added together, and these multi-season transients (MSTs) are removed from the list of potential spectroscopic follow-up targets. Objects with a positive transient_status flag in one observing season are labeled as single-season transients (SSTs), and form the set of candidates of likely SNe that become possible targets for spectroscopic follow-up programs.

3.4. *Host Galaxies*

Host galaxies are assigned to candidates via the Directional Light Radius method (DLR; Gupta et al. 2016). The DLR method uses the `SExtractor` model-independent shape parameters A, B, and $THETA$ derived from the second moments of the observed galaxy light distribution. Using these `SExtractor` parameters, we determine the distance between the candidate and the galaxy in normalized units of the light profile projected in the direction of the transient ($d_{\rm DLR}$). This quantity is computed for all galaxies within a $15''$ radius. The closest galaxy in this dimensionless measure is assigned as the likely host, provided $d_{\rm DLR} \leq 4$. If no galaxy satisfies this criterion, the candidate is considered to be hostless. We note that for all DES candidates with an identified host galaxy via the DLR method, the same galaxy would have been selected as the likely host in 98.8% of cases if we simply chose the galaxy with smallest angular separation from the candidate.

We do host-galaxy matching using the DES SVA1-GOLD galaxy catalog, created from DES Science Verification data, for DES-SN host galaxies. Although deeper catalogs can be created from subsequent data, SVA1-GOLD has the advantage of using the same catalog for all DES-SN seasons and being free of contaminating SN light. Furthermore, these catalogs are complete to $r \approx 24.4$ mag ($r \approx 25.5$ mag in the deep fields) which, as will be described in Section 4, means they are more than adequate for the purposes of our live-SN and host-galaxy spectroscopic programs.

3.5. *Photometric Classification*

During the DES observing seasons we run the Photometric Supernova IDentification software (`PSNID`; Sako et al. 2011) for every active candidate. `PSNID` compares the light curve for each candidate to a grid of templates of the most common SN subtypes (SN Ia, type II SNe, and type Ib/c SNe), measuring the best-fit parameters for each of the models to the data. It then computes the probability that the model describes the data ('FITPROB'), and uses this to determine the Bayesian probability of the candidate being a particular subtype ('PBAYES'). This information is updated with each new epoch of photometry until the end of the observing season in which the candidate was discovered. The results of `PSNID` help shape our spectroscopic SN-follow-up program (Section 4) up to and just past peak brightness for the candidate; afterward, these preliminary typings contribute to target-selection for the host-galaxy spectroscopic follow-up. We run `PSNID` in two modes: both without any priors and with a photo-z prior from the host galaxy where one has been identified. We used the DESDM neural network

photo-z catalog for these galaxies, which is described by Sánchez et al. (2014).

3.6. *Statistics Summary*

In Table 3 we present statistics describing the quantities of objects, candidates, and *transients* found in each of the first three seasons of DES. We discovered 12,015 single-season *transients* over the first three seasons of DES-SN, an average of 24 per night (see mean observing season duration in Section 2.5).

The differences in statistics between seasons are quite small, with $\mathcal{O}(10\%)$ variation among seasons. We note that candidates observed across multiple seasons—e.g., active galactic nuclei (AGN)—are attributed to the first season they appear in. As such, Y1 has a much higher number of candidates than the other seasons, but a consistent number of SSTs.

Our requirement of multi-epoch detection for all spectroscopic targeting, when coupled with the DES-SN cadence of > 6 days, limits our ability to obtain early-time follow-up spectra of transients. However, the value of the multi-epoch requirement for cleanly removing asteroids from our SN Ia follow-up sample can be clearly demonstrated. The DES-S and DES-X fields have the greatest proximity to the ecliptic, where asteroids are most likely to be detected. In S1+S2 the number of candidates per field was 250% that of the further-removed shallow fields (C1, C2, E1,and E2); for X1+X2 the rate was 192%. However, all shallow field pairs have the same number of *transients* to within 5%, as expected once asteroids are removed.

4. SPECTROSCOPY

In this section we give a full overview of the supernova spectroscopy program for the first three seasons[3] of DES-SN. First we describe in Section 4.1 the multi-pronged strategy for the live SN follow-up program and the importance of each individual component. We detail all spectroscopic observations taken of DES SN candidates, sorted by observatory and including a description of the selection criteria used, in Section 4.3. We describe our spectroscopic reduction and classification methods in Section 4.4, and present our final sample of classified DES SNe in Section 4.5. In Section 5 we will take the observations described in this Section and turn to the question of deriving the effective spectroscopic selection function of the survey.

4.1. *Supernova Follow-up Strategy & Target Selection*

The differentiating characteristic of DES-SN when compared to all previous SN Ia programs is that the primary cosmological analysis is designed for a sample of photometrically classified SNe Ia, allowing for a more efficient usage of the survey data than relying solely on spectroscopic confirmations. However, spectroscopy is still vital for DES-SN, but with a different set of priorities compared to previous surveys. Rather than our final sample consisting solely of transients classified as

SNe Ia via our spectroscopic program, the photometrically classified sample will be shaped by the redshifts and classifications obtained via spectroscopy.

The spectra collected as part of our SN Ia follow-up program serve several purposes. They constitute a truth sample for training photometric classification in DES; they are used for further analysis of detailed properties, such as the correlation between intrinsic color and velocity (Foley & Kasen 2011; Foley et al. 2011); and they provide a sample of SNe Ia in low-luminosity galaxies that would otherwise be missed by our spectroscopic follow-up program of SN host galaxies, allowing a study of systematics due to correlations between SNe Ia properties and the mass of their host galaxies (Sullivan et al. 2010; Kelly et al. 2010; Lampeitl et al. 2010). Most crucially, though, they allow for a cosmological analysis in the traditional mold of a spectroscopically confirmed SN Ia sample, testing the quality of our data and our analysis techniques. Here we describe the different modes of our spectroscopy program, and how we implemented them in order to achieve these goals.

4.1.1. *Host-Galaxy Spectroscopy*

The focus of this paper is the *live* spectroscopy of SNe in DES, but due to its outsize importance we briefly describe here the DES-SN host-galaxy spectroscopic follow-up program.

Live follow-up of SNe not only provides a spectroscopic classification of the transient, but the redshift of the object being characterized as well. For precision measurements of cosmological parameters with photometrically classified SNe Ia, DES-SN requires spectroscopic redshifts for these transients. Obtaining spectroscopic redshifts from host galaxies as opposed to the SN spectra themselves is much more efficient: the observations are not time-critical, the source density increases with time, and the targets can be repeatedly observed to obtain higher SNR and depth. Thus, the primary source of redshifts for DES-SN transients is from their host galaxies.

Most of these redshifts are obtained via the 'OzDES' survey (PI C. Lidman). OzDES began in 2013 with the primary goal of obtaining the host-galaxy redshifts necessary for DES SNe Ia cosmology. This is a 100-night program, spread over 6 years, using the 3.9m Anglo-Australian Telescope (AAT). There are 392 fibers on the AAOmega/2dF multi-fiber spectrograph covering a field of view that is nearly identical to the footprint of DECam. This allows us to obtain spectra of tens of thousands of targets across the DES-SN fields, repeatedly observing galaxies over multiple observing runs until sufficient SNR is built up to obtain a secure redshift.

Minimal cuts are placed on selecting candidates for host-galaxy follow-up: it must have an observed peak during a DES observing season, peak SNR> 5 in at least two different filters, and be a single-season transient (as defined in Section 3.3). The likely host galaxies for these transients are identified, and those with a magnitude $r < 24$ (measured within the $2''$ fiber diameter of 2dF) are selected. A full description of the OzDES observing strategy, including target classes, a list of observations, and the public spectroscopic catalog can be found in Yuan et al. (2015) and Childress et al. (2017).

We note that not all host-galaxy redshifts were ob-

Table 3
DES-SN Detection Statistics

Type[1]	Total	Y1	Y2	Y3	Deep[2]	Shallow[2]
Objects[a]	4.88M	1.63M	1.66M	1.59M	265K	137K
ML Objects[b]	1.21M	421K	389K	397K	52,623	37,139
Candidates[c]	45.9K	18,489	13,586	13,836	1100	1626
Transients[d]	17,215	6404	5521	5290	731	527
SSTs[e]	12,015	4059	4326	3630	593	347

[1] All types are defined in Section 3.3.
[2] Mean quantity per field type, per season.
[a] Detection in a single filter-epoch by `DiffImg`.
[b] Objects with (`autoScan` score ≥ 0.5).
[c] Spatially coincident detections.
[d] Candidates consisting of ML Objects on multiple epochs.
[e] Transients with 'transient_status' > 0 in one season only.

tained by the OzDES survey. OzDES assembled a custom redshift catalog in the DES-SN fields from an exhaustive literature search, which enabled the survey to more efficiently allocate its fibers by avoiding galaxies with already known spectroscopic redshifts. Additionally, live SN follow-up is often able to obtain a spectroscopic redshift from the host galaxy. However, in this latter case we still observe the host galaxy with AAT once the SN has faded to obtain a galaxy spectrum free of contaminating SN light.

4.1.2. *Magnitude-Limited Sample*

We now describe the first of our three live follow-up programs of SNe Ia. A magnitude-limited sample is a useful component for a spectroscopic supernova survey in that it creates an easily quantifiable selection function; if the resources allowed, we would carry out magnitude-limited follow-up to the full depth of our survey. We thus created a Magnitude-Limited program to characterize the brightest SN candidates in DES in an otherwise unbiased manner. No `PSNID` probabilities are used in this selection; all SSTs detected by DES are eligible to be targeted with this program. This is to later allow for testing and validation of photometric-classification routines.

The primary source of observations for this program was also the OzDES program, as it is efficient for targeting objects with a low source density (Section 4.1.1) and is rapidly configurable, allowing the target list to be updated in real time. On any given OzDES observing night, all active SSTs with $r < 22.7$ or $i < 22.7$ mag in the field being observed have a fiber placed on them. These observations were supplemented by follow-up with other observatories—primarily the Southern African Large Telescope (SALT) and MMT—to obtain classifications of SSTs not obtained at the AAT owing to weather, observing cadence, or other classification inefficiencies. The goal for completeness in this campaign was all SSTs brighter than $r = 22$ mag, though as we will demonstrate later this goal was not achieved.

4.1.3. *Faint Hosts*

Since the inclusion of a SN in the photometric cosmology analysis requires a spectroscopic redshift, all SNe occurring in galaxies too faint for our OzDES host-galaxy spectroscopy campaign ($r > 24$ mag) would be excluded from our cosmology sample. This creates a selection bias against SNe Ia as a function of both decreasing host-

galaxy mass as well as increasing redshift. To characterize this bias we carried out a follow-up program for spectroscopically classifying SNe Ia in faint host galaxies, ensuring that these SNe Ia can be retained in our final analysis. The redshift information obtained from the spectrum can be used alone or in conjunction with the spectroscopic classification.

SN Ia candidates for this program are selected based on their early-time light curve with `PSNID`, and prioritized based on the apparent faintness of their host-galaxy. There is overlap between this program and the Magnitude-Limited one, as a bright candidate can also be hostless. In these cases resources from either campaign can be used to secure a spectroscopic type. The Faint Hosts program (which targets SNe in faint galaxies, not the galaxies themselves) had dedicated observing time at the Very Large Telescope (VLT) and the Gran Telescopio Canarias (GTC), and additional data were taken with Keck and Magellan.

4.1.4. *Representative Sample*

The last of the three live SN Ia follow-up programs in DES-SN is designed to obtain a representative sample: a spectroscopically confirmed sample of SNe Ia that evenly samples the redshift distribution of SNe in the final photometrically classified analysis. This sample has many important uses, such as allowing us to test for environmental dependence and color evolution of spectroscopic properties with redshift. Quantifying the effect of evolution in spectroscopic properties on a representative sample is likely to be helpful in our future DES cosmology analysis of a photometrically classified SN Ia sample, which will lack this spectroscopic information. Having a representative sample of SNe is also important as a training set for future methods of photometric classification that rely on machine learning.

For this follow-up program, we first determine likely SN Ia candidates using `PSNID` fits. The other follow-up programs independently fill portions of this parameter space; e.g., low-redshift SNe for the Magnitude-Limited sample and (preferentially) high-redshift SNe for the Faint Host sample. As a result, the Representative Program primarily observes SNe Ia at redshifts $0.3 < z < 0.7$, and is biased toward higher-mass hosts at high redshift, areas that are missed by our other follow-up programs. Dedicated observing programs at Gemini and Magellan comprise the majority of this sample,

though data for this was collected at Keck and MMT as well. The final sample for this program should be thought of as a subset of data from all live SN programs.

4.1.5. *Non-Ia Supernovae*

DES is a cosmology survey, and thus DES-SN has been designed to discover, measure, and confirm SNe Ia. But as a deep and wide transient survey, there are many other interesting types of transients that can be found in the data. We briefly note here three additional classes of transients for which we have made a concerted effort to obtain follow-up spectroscopy: superluminous supernovae (SLSNe), tidal disruption events (TDEs), and type II supernovae (SNe II).

These programs are much smaller than our SN Ia program, with the only follow-up time specifically allocated for such observations coming from the VLT (SLSNe), Magellan (SN II), and Gemini (SN II). However, since SLSNe occur preferentially in very low-mass galaxies, we have also obtained spectral confirmations of these objects from our faint-host program. We have also unintentionally classified SLSNe with other SN Ia dedicated programs (DES15E2mlf; Pan et al. 2017), but no SNe Ia were classified from observations of potential SLSN targets. Although non-Ia SNe were observed as part of the DES-SN follow-up program, further discussion and publication of these spectra are reserved for papers analyzing these data (Papadopoulos et al. 2015; Smith et al. 2016; Pan et al. 2017; Smith et al. 2018).

4.2. *ATC*

To successfully carry out our multiple spectroscopic observing programs across a globally distributed collection of telescopes requires real-time coordination, long-term transient monitoring, and centralized data storage. For this purpose we developed a tracking database and web application called ATC, hosted at the National Energy Research Scientific Computing Center (NERSC).

Information about each DES transient, including coordinates, photometry, discovery date, and host-galaxy association, are used to seed an initial portfolio. This portfolio develops over time as additional photometry is acquired, with light-curve fits and SN subtype probabilities continuously updated using PSNID. Spectroscopic follow-up is coordinated and scheduled through ATC, as tags are applied to portfolios to indicate which transients should be observed, when, and from where. Finder charts from DECam imaging are generated on demand and made available to observers via the web. After follow-up, tags are updated and observing reports attached to the ATC. Reduced spectra are uploaded for inspection and science use by the collaboration. Redshifts and classifications derived from the spectra are recorded in ATC for each transient. All of the DES-SN spectroscopic follow-up, which we detail in the following section, was dependent on the ATC.

4.3. *Data*

Here we describe the observing campaigns undertaken by DES as a function of observatory, including the number of candidates observed, mode of observations, and resulting classifications from each telescope. In Table 4 we list the main details of the spectroscopic programs for which DES SN Ia targets were observed. We note that total allocated time, not on-sky time, is listed here. The fraction of time used on DES-SN targets varies depending on weather, observatory down time, and other programs sharing the same time allocation. Additionally, the number of spectra is the total number of observations, including repeated observations of the same target and non-Ia SNe. Thus, a comparatively low number of SN Ia classifications for a given program does not equate to a low classification efficiency. A description of the classification procedures will be given in Section 4.4.

In Table 5 we present our observation log of spectra taken of DES transients (full table is available online). For each observation we list the DES transient name; the telescope, instrument, exposure time, and setup; the MJD and UT date of the observation; the seeing and airmass; the magnitude of the transient at the time of observation; and the % increase of the flux from the transient over the background flux. We note the majority of the table consists of OzDES follow-up; there are over 1000 spectra of transients taken as part of OzDES, and 343 spectra from all other telescopes in our program combined.

Except where otherwise noted, all spectra described herein have been reduced using standard routines with IRAF (Image Reduction and Analysis Facility[4]). Basic data calibration (bias/overscan subtraction, flux calibration, and wavelength calibration) was performed by the individual observing teams. Supernova spectra were extracted from the geometrically corrected two-dimensional (2D) spectra, often with significant amounts of host-galaxy background; for higher-redshift targets embedded in their hosts, modest spatial-width apertures were used in extracting the supernova spectra to minimize host contamination.

4.3.1. *Anglo-Australian Telescope (AAT)*

The majority of spectroscopic observations of DES transients have been performed as part of the OzDES Survey (Section 4.1.1; Yuan et al. 2015; Childress et al. 2017). OzDES uses the 2dF fiber positioner on the 3.9 m AAT telescope at Siding Spring Observatory in Australia. The rapidity of the AAT fiber configuration software allows for same-day updates to the target list. We placed active transients at highest priority (i.e., over-riding all other classes of target allocations) into each observation. In Y1 and Y2 all active transients with $r < 22.5$ mag were added to the OzDES observing queue. In Y3 this was extended to objects with $i < 22.5$ mag (for any r), as well as rising transients (brightened by > 0.3 mag between detections) that were brighter than 23.0 mag in either r or i. In practice, a complete sample of bright transients was not obtained, as the time between observing runs (typically > 1 month) and weather prevented all transients from being observed with any magnitude cutoff. However the biases are still minimal, as the follow-up campaign was not influenced by any inferred supernova properties (e.g., color, light-curve shape, host properties).

---

[4] IRAF is distributed by the National Optical Astronomy Observatory, which is operated by the Association of Universities for Research in Astronomy (AURA) under a cooperative agreement with the National Science Foundation.

Table 4
DES-SN Spectroscopy Program

Observatory	PI[a]	Instrument	Wavelength [nm][b]	Allocation[c]	Season	Spectra[d]	Spec Ia[e]
AAT[f,g]	C. Lidman	2dF/AAOmega	380-880	48n	Y1,Y2,Y3	1002	77
AAT[g]	C. Smith	2dF/AAOmega	380-880	2n	Y1	7	1
Gemini[g,i]	R. Foley	GMOS	520-990	18h	Y1	2	2
Gemini[i,j]	R. Foley	GMOS	520-990	39.6h	Y3	25	18
Gemini[i]	L. Galbany	GMOS	520-990	10h	Y3	5	1
GTC	F. Castander	OSIRIS	480-920	54.6h	Y1,Y2,Y3	19	10
Keck[g]	A. Filippenko	DEIMOS	455-960	4n	Y1,Y2,Y3	7	2
		LRIS	340-1025	11.5n + 26h	Y1,Y2,Y3	18	9
Magellan	R. Kirshner	LDSS3	425-1000	2n	Y2,Y3	16	5
		IMACS	390-1000	8n	Y2,Y3	41	28
Magellan	S. González-Gaitán	LDSS3	425-1000	4n	Y3	23	9
Magellan	D. Scolnic	LDSS3	425-1000	1n	Y3	8	7
MMT	R. Kirshner	BCS	330-850	7n	Y2,Y3	31	12
SALT	M. Smith	RSS	385-820	41.59h	Y1,Y2	21	6
SALT	E. Kasai	RSS	385-820	37.5h	Y3	31	12
VLT[f,h]	M. Sullivan	X-Shooter	300-2480	14.1n	Y2,Y3	89	47
VLT[h]	M. Sullivan	X-Shooter	300-2480	12h	Y3	7	2

[a] Program IDs for the spectroscopic campaigns listed here can be found in the acknowledgements.
[b] Wavelength range given is representative of the typical instrumental setup and may vary in a given program.
[c] Actual on-sky time for each program is less than the allocation, depending on weather conditions; the priority level assigned to ToO programs; and the availability of suitable targets. Hours are used for queue-scheduled time, nights for classical time.
[d] Number of spectra obtained for DES transients by the program. Does not refer solely to SN Ia candidates.
[e] Discovery spectra only. Some programs obtained classifiable SN Ia spectra for previously classified objects; we do not double-count those here.
[f] Allocation listed is part of a long-term program that continues into subsequent seasons.
[g] Program includes DES SN Ia targets, but is not the primary purpose of the program.
[h] Data from the NIR arm not used in most observations.
[i] Observations made with Gemini-South
[j] Observations made with Gemini-North.

Table 5
Spectroscopic Observing Log: DESY1-Y3

Transient Name	Telescope	Instrument	Date [UT]	Date [MJD]	Exposure Time [s]	Seeing [arcsec]	Airmass	Slit[a] [arcsec]	Observed[b] Mag$_i$	% Flux[c] Increase
DES13C1c	AAT	AAOmega/2dF	2013-10-01	56566.66	3x2400,1x1800	2.5-5	....	2.0	22.3 [0.6]	116.0
DES13C1d	AAT	AAOmega/2dF	2013-10-01	56566.66	3x2400,1x1800	2.5-5	....	2.0	23.7 [0.6]	9.79
DES13C1e	AAT	AAOmega/2dF	2013-10-01	56566.66	3x2400,1x1800	2.5-5	....	2.0	21.9 [-7.5]	50.0
DES13C1eie	AAT	AAOmega/2dF	2013-11-30	56626.71	1x2400	NA	....	2.0	24.1 [1.4]	7.43
DES13C1eie	AAT	AAOmega/2dF	2013-12-01	56627.65	2x2400,1x1596	1.6	....	2.0	24.1 [0.4]	7.43
DES13C1feu	SALT	RSS	2013-10-08	56573.91	1x2400	1.2	1.18	1.5	19.9 [1.3]	140.0
DES13C1feu	AAT	AAOmega/2dF	2013-10-30	56595.68	2x2400	1.3	....	2.0	20.9 [-5.3]	31.8
DES13C1feu	AAT	AAOmega/2dF	2013-11-02	56598.69	2x2400	1.6	....	2.0	21.2 [3.4]	24.1
DES13C1feu	AAT	AAOmega/2dF	2013-11-30	56626.71	1x2400	NA	....	2.0	22.0 [1.4]	11.6
DES13C1feu	AAT	AAOmega/2dF	2013-12-01	56627.65	2x2400,1x1596	1.6	....	2.0	22.0 [0.4]	11.6
DES13C1feu	AAT	AAOmega/2dF	2013-12-26	56652.63	1x2400	1.3	....	2.0	22.7 [0.5]	6.07
DES13C1fpp	AAT	AAOmega/2dF	2013-10-30	56595.68	2x2400	1.3	....	2.0	>21.9 [-5.3]	<19.4
DES13C1gki	AAT	AAOmega/2dF	2013-10-30	56595.68	2x2400	1.3	....	2.0	22.9 [-1.5]	260.0
DES13C1gol	Keck	DEIMOS	2013-10-06	56571.53	1x1200	0.6	...	...	22.5 [3.7]	117.0
DES13C1hwx	AAT	AAOmega/2dF	2013-10-30	56595.68	2x2400	1.3	....	2.0	22.6 [-1.5]	885.0

Note. — This table is available in full online as part of the DES-SN3YR data release: https://des.ncsa.illinois.edu/releases/sn

[a] For AAOmega/2dF, fiber diameter is given in place of slit width.
[b] Apparent magnitude from DES-SN observation on the epoch t_{phot} closest to the time of spectroscopic followup t_{spec}. In brackets we give the value of $t_{phot} - t_{spec}$.
[c] Brightness of target at time of observation relative to the surface brightness of the background.

AAT observations form the majority of our Magnitude-Limited sample described in Section 4.1.2, as well as the Host-Galaxy program detailed in Section 4.1.1. Observations were made using the AAOmega dual bench spectrograph with the 2dF fiber positioners (Saunders et al. 2004; Smith et al. 2004). The AAOmega setup consisted of the x5700 dichroic with 580V (blue) and R385 (red) gratings, with a resulting continuous wavelength coverage of $3800-8800$ Å. Both CCDs were upgraded between Y1 and Y2, resulting in better quantum efficiency in both arms, as well as fewer cosmetic defects in the blue and less fringing in the red. The 2dF instrument places 392 science fibers, each with a diameter of $2''$, over a 2-degree diameter field. The spectra were reduced with a modified copy of v6.2 of the 2dfdr pipeline (Croom et al. 2004), which is further described by Childress et al. (2017).

Over the course of the first three DES observing seasons (Y1/Y2/Y3) OzDES was allocated 48 nights

(12/16/20); a further two nights allocated in Y1 to another DES AAT program (PI C. Smith) were integrated into OzDES, both operationally and in terms of data reduction. We obtained 1009 spectra (235/307/467) of 533 (127/180/226) distinct transients[5]. For over half of the transients (274) we obtained a single spectrum, while for approximately half of the remainder (128) we obtained multiple spectra in one observing run. Thus, while most transients (402) were observed in only one run, 99 were observed in exactly two runs, and 32 were observed in three or more runs. The typical gap between observing runs was approximately one month.

The total numbers of supernovae spectroscopically confirmed with OzDES are 78 SNe Ia (12/26/40), 14 SNe II (3/3/8), and 1 SN Ic (1/0/0). The median redshift of SNe Ia classified by OzDES is $z = 0.279$. Spectroscopic classification efficiency with this program is very low owing to the observational setup: $2''$ diameter fibers mean more host-galaxy light than SN light typically enters the fiber, and our follow-up strategy does not take into account the increase over background surface brightness. Unlike our other spectroscopic follow-up programs, transients were not removed from the OzDES queue once they possessed a spectroscopic classification. Therefore, we have classification-quality spectra from OzDES for an additional 36 transients which we do not consider as 'classified' by OzDES.

4.3.2. Gemini

We obtained 32 spectra of 29 DES transients using the Gemini Observatory; 18 spectra taken at the 8.1 m Gemini North telescope on Maunakea, Hawaii, and 14 spectra taken at the 8.1m Gemini South telescope on Cerro Pachon, Chile. Observations were carried out in long-slit mode with the Gemini Multi-Object Spectrograph (GMOS; Hook et al. 2004), one of which is present on each telescope. With the exception of two spectra in Y1, all of our observations presented here were made in Y3, after the upgrade to Hamamatsu CCDs on GMOS-S (2014A), but prior to the upgrade on GMOS-N (2017A). All but one target were observed with the R400 grating, which yields $\lambda/\Delta\lambda = R \approx 1900$. Order-blocking filter OG515 was used in most observations, yielding a useful wavelength range of $5200 - 9900$ Å, and the standard slitwidth was $1.0''$. Full details for each spectrum can be found in Table 5 online. We note that all data with Gemini were taken in queue mode.

Gemini was the primary resource used for our Representative sample, though one of our programs was also part of the Non-Ia program. We classified 21 of 29 objects targeted as SNe Ia (median $z = 0.565$), 2 as SNe Ibc, and one as a SLSN. All transients were initially targeted as likely SNe Ia including the high-z SLSN DES15E2mlf (Pan et al. 2017), which was also the only transient observed multiple times with Gemini.

4.3.3. GTC

We obtained 19 spectra of 18 DES transients using the Optical System for Imaging and low-Intermediate-Resolution Integrated Spectroscopy (OSIRIS; Cepa et al.

[5] In early versions of the `DiffImg` pipeline artifacts were not efficiently vetoed. This led to candidates targeted by OzDES in Y1 which were later identified as artifacts. For clarity we include here numbers referring only to real transients.

2003) on the 10.4 m GTC located at the Observatorio del Roque de Los Muchachos in La Palma. All observations were made in long-slit mode using the R500R grism, yielding $R \approx 600$ with a useful data range of $4800 - 9200$ Å. All but one observation used a $0.8''$ slit. Observations took place over all three seasons, with 5/9/5 targets in DES Y1/Y2/Y3. All observations were carried out in queue mode.

We primarily used GTC for our Non-Ia and Faint Host programs. We classified 10 SNe Ia (median $z = 0.398$) and 5 SLSNe with GTC. The remaining observations were re-observations of previously classified targets (one SN Ia, one SLSN, and one TDE). Only one target was not classified.

4.3.4. Keck

We obtained 25 spectra of 23 DES transients using instruments at the 10 m W. M. Keck Observatory on Maunakea, Hawaii. Seven spectra of distinct targets were obtained with the DEep Imaging Multi-Object Spectrograph (DEIMOS; Faber et al. 2003) on Keck II, and 18 spectra of 16 transients were followed up with the Low Resolution Imaging Spectrograph (LRIS; Oke et al. 1995) on Keck I. DEIMOS observations utilized the LVMslitC slitmask, typically with a $1.0''$ slit, and a combination of the low-resolution 600ZD grating ($R \approx 123$) with the GG455 long-pass order-blocking filter. This provided a useful wavelength coverage of $4550 - 9600$ Å. On LRIS the 600/4000 grism was used on the blue side and the 400/8500 grating was used on the red side, providing a wavelength coverage of $3400 - 10250$ Å. Most observations used the $1.0''$slit rotated to the parallactic angle to minimize the effects of atmospheric dispersion (Filippenko 1982; in addition, LRIS has an atmospheric dispersion corrector). Observations took place over all three seasons, with 4/12/9 targets in DES Y1/Y2/Y3. All observations with Keck were taken as part of classically scheduled time.

Observations with Keck primarily were part of the Representative (17 targets) and Non-Ia (6) programs. We classified 11 SNe Ia (median $z = 0.443$), 1 SLSN, 1 SN II, and 1 SN IIn with Keck. We took multiple spectra of a SLSN and a TDE. Non-classifications were mainly due to poor observing conditions. The data were reduced using standard techniques with routines written specifically for Keck+LRIS in the Carnegie `python` (`carpy`) package (Kelson et al. 2000; Kelson 2003)."

4.3.5. Magellan

We obtained 88 spectra of 86 transients in DES using the twin 6.5 m Magellan telescopes at Las Campanas Observatory, Chile. 47 spectra were obtained on the Low Dispersion Survey Spectrograph (LDSS-3) on the Clay Telescope, while 41 were obtained with the Inamori Magellan Areal Camera and Spectrograph (IMACS; Bigelow et al. 1998) on the Baade Telescope. IMACS observations were made in Short Camera Mode with the Gri-300-17.5 grism, providing wavelength coverage over $4250 - 9500$ Å with resolution $R \approx 1100$. Various slit widths as well as slit masks were used, though no observations were made in MOS mode. LDSS-3 data were taken with three different observing programs, but all observations were made with the VPH-ALL grism, covering the wavelength range

$4250-10000$ Å with $R = 860$. No observations with Magellan occurred in Y1, increasing to 31 and 57 in Y2 and Y3, respectively. All observing time used was classically scheduled.

Observations with Magellan were split amongst nearly all programs, with targets falling in the Representative, Magnitude-Limited, and Non-Ia samples. We classified 49 SNe Ia (median $z = 0.348$), 6 SN II, 1 SN Ibc, and 1 TDE with Magellan. The only targets with multiple spectra were a previously classified SLSN, a TDE, and a SN Ia candidate previously observed in poor conditions.

4.3.6. MMT

We obtained 31 spectra of 28 DES transients using the Blue Channel Spectrograph (BCS; Angel et al. 1979) on the 6.5 m MMT at the Fred Lawrence Whipple Observatory in Mount Hopkins, Arizona. All observations are single-slit and utilized the 300GPM grating and a clear filter, with a resolution $R = 740$ covering a wavelength range of $3300 - 8500$ Å. Most observations used the $1.0''$ slit. A majority of the spectra (22) were taken in Y2, with the remainder coming in Y3. All observing time was classically scheduled.

Observations with MMT were primarily part of the Magnitude-Limited sample, with a few targets in both the Representative and Non-Ia samples. We classified 12 SNe Ia (median $z = 0.302$), 1 SN II, and 1 SLSN-I with MMT. Non-classifications were primarily due to poor weather and targets in the Magnitude-Limited sample having significant host-galaxy contamination. The three targets observed twice were SN Ia candidates for which initial spectra were of low SNR.

4.3.7. SALT

We obtained 52 spectra of 44 distinct DES transients using the Robert Stobie Spectrograph (RSS; Smith et al. 2006) on the 11 m SALT at the South African Astronomical Observatory (SAAO). All observations were made in long-slit mode using the pg0300 low-resolution grating ($R \approx 350$) and the pc03850 UV order-blocking filter. The extracted spectra cover a wavelength range of $3850 - 8200$ Å. Most observations were carried out using a $1.5''$ slit, which is well matched for the typical seeing at the site. We have observed DES transients with SALT in every DES season, with 10/6/28 targets in Y1/Y2/Y3, respectively. All Observations were carried out in queue mode.

Observations with SALT mainly belong to the Magnitude-Limited sample. We classified 18 SNe Ia (median $z = 0.175$), 3 SNe II, 2 SNe Ic, and 2 SNe Ibc with SALT. This program had an additional goal of obtaining SN Ia spectra near maximum light for a detailed analysis project; this led to us obtaining spectra of SNe Ia that already had classifications. Most repeat observations of a transient were due to the fixed zenith angle of the telescope, which results in a limited visibility window and led to us obtaining multiple observations to increase the effective SNR. The only exception was DES15S2nr, a SLSN that was observed several times with SALT. Data were reduced using PySALT[6], the SALT science pipeline (Crawford et al. 2010).

[6] http://pysalt.salt.ac.za

4.3.8. VLT

We obtained 96 spectra of 91 DES transients using the X-Shooter echelle spectrograph (Vernet et al. 2011) on the 8.2 m VLT at the European Southern Observatory (ESO) on Cerro Paranal, Chile. X-Shooter has three arms (UVB, VIS, NIR), which combined provide continuous wavelength coverage over $3000 - 24800$ Å. The resolution depends on the arm and slit-width used (typically $0.7 - 1.0''$), varying from $R \approx 4000 - 10000$. Most of our observations were in 'stare' mode, as the magnitude range of our targets means only the UVB and VIS arms provide useful data. However, for brighter targets we observed by nodding along the slit, which facilitates sky subtraction in the NIR arm. Spectra were taken in Y2 (38) and Y3 (58), spanning ESO observing periods P93-P96. We note that some of our observations took place before X-Shooter was moved from UT3 to UT2, after P93. Our larger VLT program (spanning 4 ESO semesters) was classically scheduled, while the smaller one was queue observing.

VLT was the primary source for our Faint Hosts program, though our queue program was targeted at SLSNe. We classified 49 SNe Ia (median $z = 0.541$), 10 SNe II, 2 SLSNe, and 1 SN Ic with VLT. Multiple spectra were obtained for two candidates with initial low SNR observations, while time-series data were obtained for two non-Ia targets. The data were reduced via a modified version of the `EsoReflex` pipeline (Freudling et al. 2013), where the rebinning procedure on the highly dispersed echelle spectrum has been improved to obtain proper statistics for very low SNR data.

4.3.9. Additional Spectra

The programs above are supplemented by a small quantity of assorted additional spectra. We obtained data with the Shane 3 m telescope at Lick Observatory confirming DES14X2fna as a SN II, which later transitioned to a SN IIb. We obtained spectra of DES14C3rap and DES14C1kia with the 4.1 m Southern Astrophysics Research Telescope (SOAR) on Cerro Pachon, Chile; the former classified as a SN Ia, while the latter had been previously classified as a TDE. We obtained via a DDT proposal a spectrum of DES13S2cmm using FORS2 at VLT, which became the first classification of a SLSN in DES (Papadopoulos et al. 2015).

Two DES transients were bright enough that classifications were made prior by other groups before we had the opportunity to obtain spectra of the candidates. DES13C3avpi was classified as a SN Ia by the PESSTO collaboration using the 3.58 m NTT (as PS1-13eao; Bersier et al. 2013), and DES14S1rwf was also classified as a SN Ia, by the KISS collaboration using the 1.88 m Okayama telescope (as SN2014dy; Matsumoto et al. 2015).

4.4. Transient Spectroscopic Classification

We classify all reduced spectra using both `SNID` (SuperNova IDentification; v5.0; Blondin & Tonry 2007) and `Superfit` (v3.5; Howell et al. 2005) software. These approaches use cross-correlation techniques (`SNID`) and chi-squared minimization (`Superfit`) to produce, for a given spectrum, a rank-ordered list of matches from a spectral library of supernovae, galaxies, or any other variable ob-

Table 6
Spectroscopically-Confirmed Supernovae in the DES-SN Three-Year Sample

Name	SNID	RA (J2000)	DEC	z	z_{err}	Classification
DES13C1feu	1251839	53.266731	-26.964838	0.05982	0.0005	SNIc
DES13C1hwx	1253039	54.418591	-27.527397	0.454	0.006	SNIa
DES13C1juw	1253920	54.629311	-27.042770	0.196	0.0005	SNIa
DES13C1ryv	1257366	53.899559	-26.969273	0.2118	0.0005	SNIa
DES13C2acmj	1262128	53.267674	-29.469212	0.1137	0.0005	SNIa
DES13C2bxd	1247673	54.510422	-29.157028	0.04042	0.0005	SNIc
DES13C2dyc	1249851	55.218029	-29.399984	0.2159	0.0005	SNIa
DES13C2jtx	1252955	54.722439	-28.774586	0.223	0.005	SNII
DES13C3abhe	1262715	53.369957	-28.442709	0.69	0.01	SNIa
DES13C3abht	1262214	53.502693	-28.660202	0.69	0.01	SNIa

Note. — This table is available in full online as part of the DES-SN3YR data release: https://des.ncsa.illinois.edu/releases/sn

jects. These codes also allow for external information, such as redshift and phase, to be included in the fit. All fits were performed using the spectroscopic redshift obtained either from galaxy emission lines in the spectrum itself or from a custom redshift catalog created from an exhaustive literature search by the OzDES team where available. The `Superfit` classification results are given priority owing to its inclusion in the fitting process of galaxy contamination in the observed spectrum.

Classifications were determined via visual inspection of the resulting rank-ordered fits by a subset of co-authors, and were based on consensus of the best-fitting templates. Spectra fall into one of the following broad categories: (i) a transient of some known type (see below), (ii) uncertain (spectrum contains some signal from a transient, but classification is unclear), or (iii) a galaxy spectrum with no obvious transient light. For the transient classification, we characterize the spectra as "SNIa", "SNIbc", "SNII", "SLSN-I", "TDE", "AGN", and "M-star". The TDE is an outlier, as this was classified by visual comparison with known TDE spectra without the use of `SNID` or `Superfit` results. Further detailed subclassifications are not attempted in the analysis for this paper, as the typical DES spectrum is only intended to have a sufficient SNR to make broad classifications required for distinguishing SNe Ia from other types. Peculiar subtypes of SNe Ia are mostly rejected in the light-curve fitting process, which will by necessity be the only method of rejecting these transients from the photometric-cosmology analysis as well. Detailed subsets of SNe spectra with higher SNR will be analyzed in future DES papers.

Both the spectroscopic redshift and the phase of the SN, as determined from the light-curve evolution, must match the entire list of best-fitting templates for a definitive classification to be claimed. If no spectroscopic redshift from the host galaxy is available, then the SN redshift can be fit as well, and a definitive classification can be claimed if the phase, type, and redshift are robustly determined by the fitting software.

Where a classification is highly probable but with some (well-defined) uncertainty, we use the following classifications: "SNIa?", "SNIbc?", "SNII?", and "SLSN-I?". These classifications are used in two cases. The first case is when there is no independent host-galaxy prior on the redshift and a small fraction of viable fits exists with a redshift and/or type that differs from the primary classification. The second case is where a spectrum is a good

fit to templates over only one half of the spectrum for plausible reasons: a low-SNR spectrum, poor sky subtraction, or host-galaxy contamination (primarily in the red portion of the spectrum, as the SN is typically brightest in the blue). The phase is still required to match the light curve in all cases. We note that in Section 4.3, for simplicity, we combined likely and definitive classifications. We describe these in more detail in Section 4.5.

4.5. *Spectroscopy Summary*

In Table 6 we present our spectroscopically classified SNe from the first three seasons of the DES-SN program. We have classified 307 SNe over a redshift range $0.017 < z < 1.86$ and a dynamic range of > 1000 in peak observed flux. We list totals for all certain and likely classifications in Table 7. Combining these, we have identified 251 spectroscopic SNe Ia, 34 SNe II (including IIn), 12 SLSNe, and 10 SNe Ib/Ic/IIb. In Figure 6 we present several of our spectroscopically classified SNe Ia with their best-fit template models overplotted.

In Figure 7 we show the redshift distribution of the SNe Ia classified by our program, color-coded by the telescope which provided the classification. The observing program that drives the follow-up for each telescope can be seen in the redshift range of classified SNe Ia in the figure. VLT (Faint Hosts) dominates at high-z, while the AAT and SALT (Magnitude-Limited) fill out medium and low redshifts. Magellan and Gemini extend from mid to high redshift owing to a mixture of Magnitude-Limited and Representative programs.

In Figure 8 we show the apparent magnitude distribution of transients targeted, and classified, as a function of telescope, where the magnitude is taken from the DES epoch immediately preceding the spectroscopic observation. Here we include *all* classifiable spectra as successes, including where the transient targeted has previously been spectroscopically confirmed. Note that while OzDES obtained nearly three times as many spectra as all the single-slit programs combined, the classification efficiency for AAT ($\sim 25\%$) was far below that of the single-slit follow-up ($> 70\%$).

We show in Figure 9 the classified vs. unclassified spectra obtained at VLT, plotted as a function of apparent magnitude, percent increase over background, and SNR (indicated by the size of the points). To compute the SNR for each spectrum we split the region $5000 < \lambda(\text{Å}) < 9000$ into 200 Å sections, and determine the root-mean square (RMS) about the best-fit line in
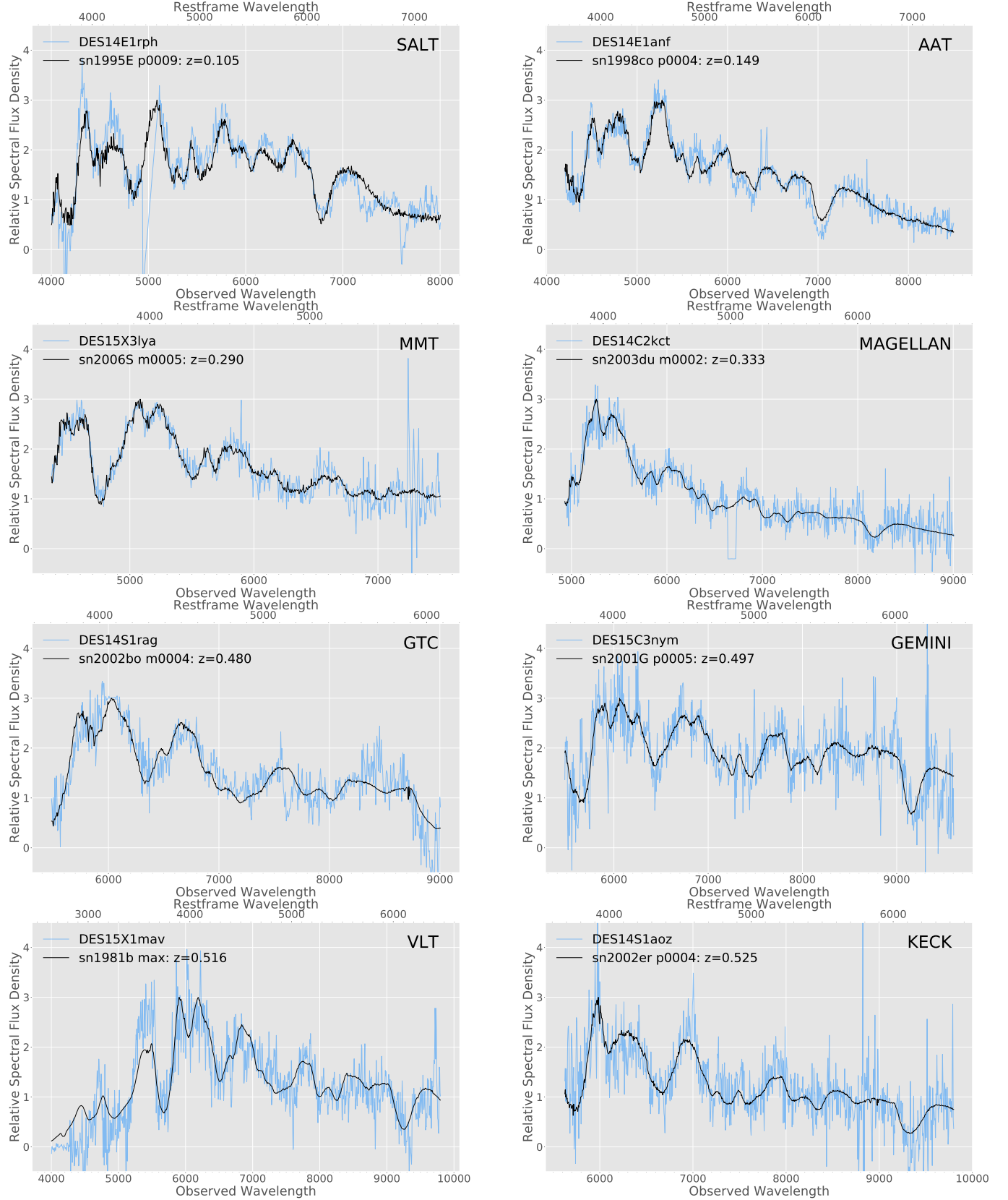
Figure 6. Observations from each of the observatories used for the DES-SN follow-up program. Spectra are plotted in blue, with the best-fit supernova template overplotted in black. Fits are derived using `Superfit`, and host-galaxy contamination has been subtracted from the data. All spectra shown here are classified as 'SNIa'.
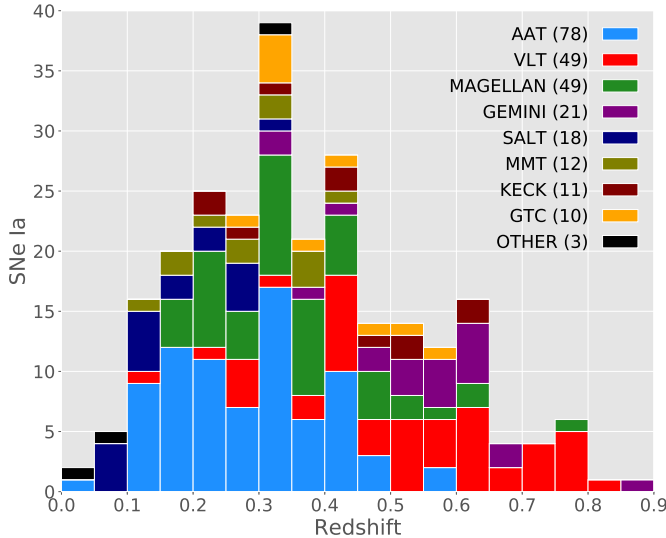
Figure 7. Redshift histogram of all 251 spectroscopically confirmed SNe Ia in the first three seasons of DES ($\Delta z = 0.05$). The histogram is split by discovery observatory, with the total quantity of SNe Ia classified by each telescope indicated in the legend.

Table 7
DES Classification Summary

Type	Classifications
SNIa	225
SNIa?	26
SNII	25
SNII?	8
SNIIn?	1
SNIIb?	1
SNIbc	5
SNIc	4
SLSN-I	11
SLSN-I?	1
TDE	1
AGN	53

each section. The SNR for the spectrum is then the average over all sections of the mean flux over RMS per section. The linear fitting accounts for the fact that a SN spectrum has broad lines and therefore the simple RMS cannot be used as an indicator of uncertainty alone. As expected, we find that the non-classified spectra tend to lie in the regime of low SNR and/or faint objects. By design there are very few transients observed with this program that are not significantly above the background. As a result our classification efficiency with VLT is high.

The number of spectroscopic classifications increased dramatically as the DES survey progressed. While the number of AAT nights increased modestly (from 10 to 12 to 16), the number of DES-SN spectra obtained from all other observatories over the first three seasons rose from 24 to 121 to 199. This expansion of resources resulted in 24/75/152 spectroscopically classified SNe Ia in DES Y1/Y2/Y3, respectively. We note that the efficiency of the survey pipeline itself also improved through the seasons; both the speed at which DES data were processed and the quality of artifact rejection increased dramatically from Y1 to Y3. These improvements also contributed to the year-on-year increase in classified SNe Ia.

5. SELECTION FUNCTION

One significant difficulty in an analysis of spectroscopically classified SNe Ia is the inherent complexity in determining how the observed sample relates to the broader set of photometric candidates: the spectroscopic selection function (SSF[7]). In an idealized case, every SN would be classified. This requires a telescope allocation large enough to target all transients, which is never realized (with the exception of very-low redshift surveys, such as ASAS-SN (Shappee et al. 2014)), and thus requires some prioritization of transients. Targeting is based on incomplete light curves. Delays are introduced if many artifacts enter the photometry pipeline, or if data processing lags for any reason. Telescope time is either classically scheduled or queue scheduled, neither of which guarantee a transient is observed at an appropriate epoch to maximize SNR and secure a classification. Observing conditions – clouds, seeing, moon phase – all play a continuously varying role as well. Available spectroscopic resources may be allocated in the wrong hemisphere for follow-up of a particular target.

In addition to accounting for the selection effects from `DiffImg`, the inefficiencies of the spectroscopic sample must also be accounted for in the cosmology-parameter analysis. Modeling all the inputs that ultimately shape our spectroscopic selection is not possible; this would have to incorporate computer failures that induced delays in data reduction as well as dust storms and instrument failures that caused prolonged shutdowns at certain observatories. Rather than attempting to model the SSF from first principles, we determine an *effective* SSF for SNe Ia in DES. In Section 5.1 we derive the SSF from our data. In Section 5.2 we use this SSF to create a DES-like simulation and compare the resulting SN Ia sample to the observed DES sample. In Section 5.3 we examine a forward-modeling approach to deriving the SSF and how that differs from the data-driven model, and in Section 5.4 we show how these SSFs affect the distance-modulus bias correction for our spectroscopic SN Ia sample.

5.1. *SSF Derivation*

The SSF is the fraction of SNe Ia identified as candidates by DES that are subsequently spectroscopically classified. Thus, the denominator of the SSF should be the subset of single-season transients (SSTs; Section 3.3) detected by DES that were real SNe Ia. Since we do not know the true classification of all SSTs from DES, we determine the likely number of SNe Ia based on the results of photometrically classifying our full three-year data sample (real-time decisions were based on classifications from rising light curves, which are less accurate than the full light curves used here). We define the SSF as a function of the peak magnitude of the transient in the observer-frame i band (m_i), which is used for most spectroscopic follow-up decisions. Thus,

$$\mathrm{SSF}(m_i) = \frac{N_{\mathrm{SpecIa}}(m_i)}{N_{\mathrm{PhotIa}}(m_i)}. \quad (1)$$

We select all 12,015 SSTs from the first three seasons of

---

[7] Referred to as E_{spec} by Kessler et al. (2018) and Brout et al. (2018a)
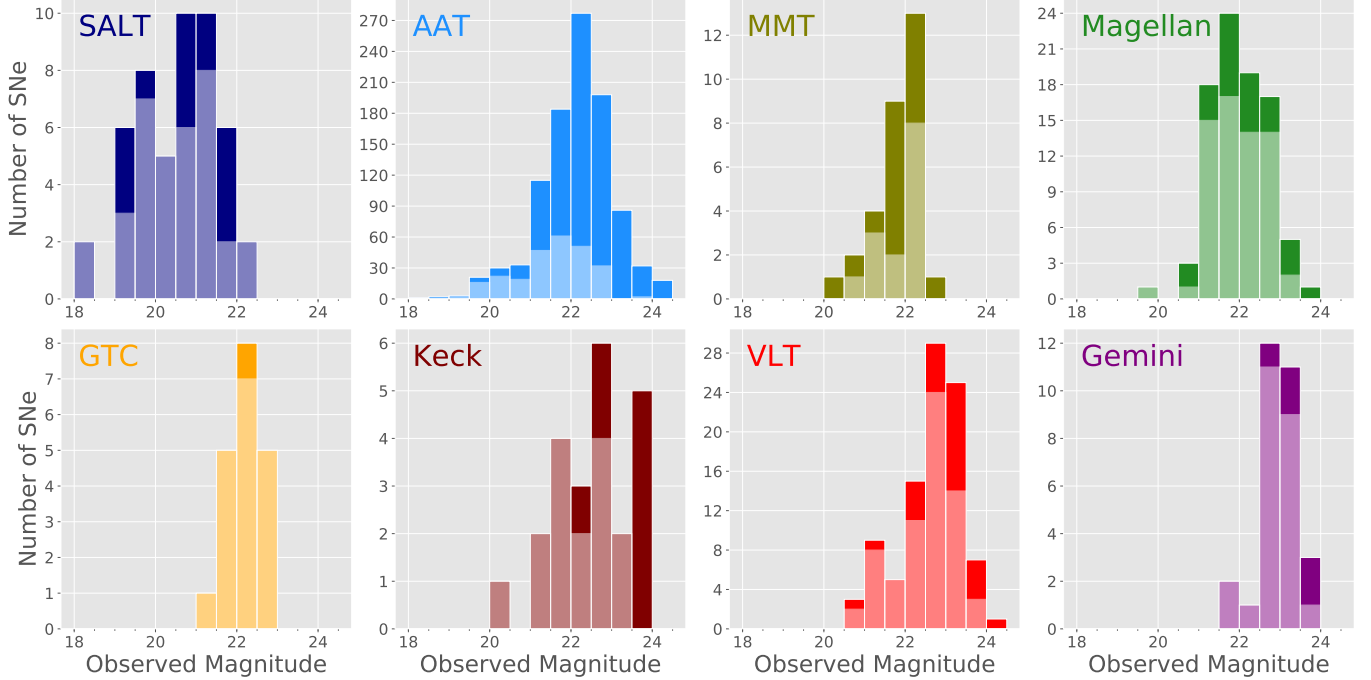
Figure 8. Observed apparent magnitude distributions for transients spectroscopically observed in the first three seasons of DES. Magnitudes are i-band for all observatories other than AAT and SALT, which were r-band selected follow-up programs. Distributions are shown separately for each telescope, in order of increasing median apparent magnitude: from $r = 20.8$ for SALT to $i = 23.0$ for Gemini. The lighter shaded histogram in each plot represents the subset of observations that resulted in a successful classification.
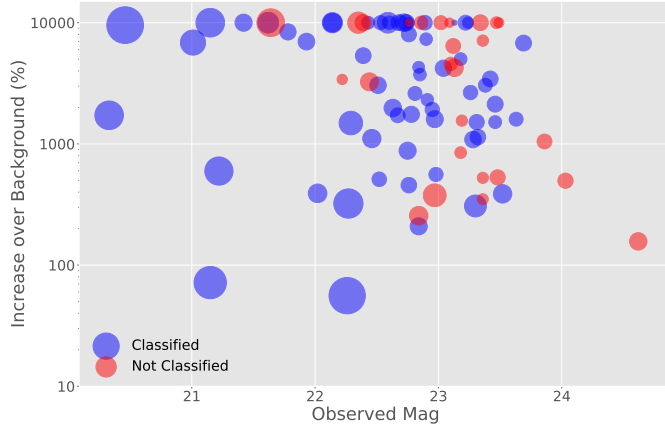
Figure 9. Observed i-band magnitude plotted against the percentage increase over background flux for each SN observed by our VLT program. SNe that are $> 10,000\%$ the brightness of their background are plotted at this value for purposes of clarity. Successful classifications are shown in blue, while non-classification are plotted in red. The size of each point is proportional to the SNR for the spectrum, with the method for computing this described in Section 4.5.

DES, and determine $\text{PBAYES}_{\text{Ia}}$ and $\text{FITPROB}_{\text{Ia}}$ using `PSNID` (Section 3.5). We use both the SN Ia light-curve models of Sako et al. (2011) as well as the set of core-collapse supernova (CCSN) templates adopted in that paper. Motivated by the cut thresholds defined by Sako et al. (2011, 2018), we select as likely SNe Ia all SSTs with $\text{PBAYES}_{\text{Ia}} \geq 0.9$, $\text{FITPROB}_{\text{Ia}} \geq 0.01$, and peak $\text{SNR} \geq 5$ in at least two bands. We note that our outlier rejection allows at most two filter-epochs of photometry to be removed from the fitting, provided they have $\Delta\chi^2 \geq 10$.

For this subset of likely SNe Ia we determine the best-fit light-curve parameters using the Guy10_UV2IR version of the SALT2 model, which was first used by Rodney et al. (2012) (for a description and a more advanced version of this model, see Pierel et al. 2018). We note that this model is defined over a wider wavelength range than the B14-JLA model (Betoule et al. 2014), providing more complete coverage of the DES filters over a wide redshift range, and thereby allowing us to constrain the peak fit magnitude for most of our candidates. We run our fits using the snlc_fit module in the "SuperNova ANAlysis" (`SNANA`) software package (Kessler et al. 2009b), using no prior for the redshift for any SN Ia candidate. We remove objects whose best-fit x_1 and color parameters are at the boundaries of our fitting range ($x_1 = \pm 4, c = \pm 1$), which typically signifies a non-convergent fit and a likely CCSN. This leaves us with 2634 photometric SNe Ia.

For the spectroscopic sample, we similarly fit each of the 251 spectroscopically classified SNe Ia with a Guy10_UV2IR model and measure the best-fit, observer-frame i-band magnitude at peak. We bin both our photometric and spectroscopic SNe Ia samples by peak i-band magnitude and divide to create our data-driven SSF, which we show in Figure 10. The spectroscopic sample in its entirety is a subset of our photometric sample.

While photometry for all DES-SN candidates has been computed from the `DiffImg` pipeline, we have also developed a photometric pipeline that forward models a variable transient flux on a temporally constant background. This 'Scene Modeling Photometry' (`SMP`; Brout et al. 2018b) has been computed for the DES-SN3YR sample and is used in our cosmology analysis by Brout et al. (2018a), but is computed *only* for these transients. For the classifications and light-curve fits described above we have used `SMP` for the spectroscopic sample, but find negligible differences in our results from using `DiffImg`
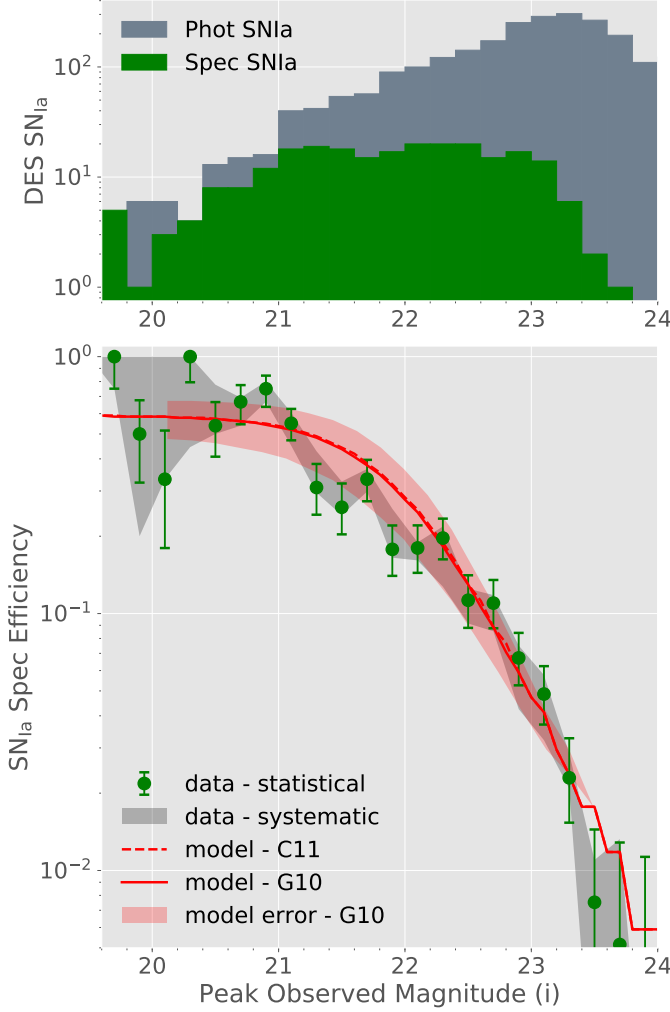
Figure 10. Top: Histogram of the number of SNe Ia spectroscopically classified (251; green) and photometrically classified (2634; grey) in this paper, as a function of peak observed i-band magnitude. **Bottom:** Data-driven SSF (green), defined as a function of peak observed i-band magnitude, derived from the data shown in the top plot. Error bars are statistical uncertainties in each bin derived from Eq. (2), and the grey band is our estimated systematic uncertainty, described in Section 5.1. In our analysis we set the efficiency to 1 at $i \leq 20.4$ mag to prevent artifacts in our derived mu-bias, as described in the text. The model-driven SSFs described in Section 5.3 are shown as solid and dotted lines depending on the assumed scatter model G10 or C11, respectively. We show the 1σ contour for the G10 derivation only, and note that the contours with C11 model are very similar. The model-driven SSF has an arbitrary normalization, which we scale here to minimize the difference with respect to the data-driven SSF.

instead. These differences are included in our systematic uncertainties, described in more detail below.

For magnitudes $m_i \leq 20.4$, we have set the efficiency equal to 1 (i.e., 100% classification rate), despite the fact that there are SNe Ia in DES brighter than this limit which have not been confirmed. We have made this choice because the SSF is ultimately used to determine how our selection creates a biased subset of SNe Ia. The bright SNe Ia that went unconfirmed were not due to any lack of brightness, but rather operational issues (lack of telescope time or processing problems). There are only a total of 34 photometric SNe Ia in this magnitude range—1.3% of the total photometric sample. We present our

Table 8
DES Spectroscopic Efficiency

Peak Mag(i)	Efficiency	σ_{stat}	σ_{sys}
20.3	1.000	+0.000/-0.205	+0.000/-0.556
20.5	0.538	+0.127/-0.131	+0.239/-0.038
20.7	0.667	+0.108/-0.121	+0.026/-0.128
20.9	0.750	+0.094/-0.113	+0.050/-0.083
21.1	0.550	+0.076/-0.078	+0.055/-0.100
21.3	0.309	+0.073/-0.067	+0.119/-0.014
21.5	0.259	+0.062/-0.056	+0.067/-0.018
21.7	0.333	+0.063/-0.060	+0.032/-0.035
21.9	0.178	+0.042/-0.038	+0.078/-0.013
22.1	0.180	+0.040/-0.036	+0.009/-0.019
22.3	0.197	+0.037/-0.034	+0.021/-0.069
22.5	0.113	+0.028/-0.025	+0.012/-0.021
22.7	0.110	+0.025/-0.022	+0.008/-0.025
22.9	0.067	+0.017/-0.015	+0.008/-0.025
23.1	0.049	+0.014/-0.012	+0.009/-0.016
23.3	0.023	+0.010/-0.008	+0.006/-0.002
23.5	0.008	+0.007/-0.004	+0.004/-0.007
23.7	0.005	+0.008/-0.004	+0.008/-0.001

Note. — For purposes of analysis, the efficiency is assumed to be 1.000 below magnitude 20.3.

derived spectroscopic selection function in Table 8.

To determine the statistical uncertainty in each bin, we follow the method adopted by Frohmaier et al. (2017) for supernova rate calculations, which draws upon Paterno (2004). In each bin the number of spectroscopic classifications k out of n detected SNe Ia is a binomially distributed variable, with the Bayesian posterior probability distribution for the rate ϵ defined as

$$p(\epsilon|k,n) = \frac{\Gamma(n+2)}{\Gamma(k+1)\Gamma(n-k+1)}\epsilon^k(1-\epsilon)^{n-k}. \quad (2)$$

We plot as our error bars in Figure 10 the 1σ uncertainties, i.e., the bounds containing 68.3% of the probability.

In deriving the selection function there were several choices made that could have been done differently. We could have fit the JLA-B14 model to determine the peak magnitude rather than Guy_UV2IR; we could have used the observed rather than fit peak magnitude; we also could have used higher or lower PSNID cut thresholds for defining a likely SN Ia. We have re-computed the SSF using each of these variations to our analysis, including in the PBAYES$_{\text{Ia}}$ (0.5, 0.99) and FITPROB$_{\text{Ia}}$ (0.001, 0.1) parameters. We define as our systematic uncertainty the maximum variation in our derived SSF in each magnitude bin, which we plot in Figure 10. We note that the systematic uncertainty is comparable to or smaller than the statistical uncertainty over nearly the entire magnitude range to which we are sensitive.

5.2. Data Comparison to Simulations

The SSF derived above comes directly from the observed data, and is not dependent on simulations or any assumptions about SN Ia rates or intrinsic parameter distributions. However, it is useful as a consistency check to determine whether our derived SSF produces a spectroscopic SN Ia sample similar in redshift distribution and SN Ia light-curve parameters to that observed when input into a DES-like simulation.

As part of the first DES-SN cosmology analysis (DES Collaboration 2018a; Brout et al. 2018a) – which uses only spectroscopically confirmed SNe Ia from the first

three years of the survey, described in this paper – we
have created a suite of simulations (Kessler et al. 2018)
that produces a highly accurate DES-like survey. We re-
fer the reader to Figure 1 of Kessler et al. (2018) for an
overview of the SNANA simulation, and list below some of
the more important assumed parameters:

- SALT2 model: Betoule et al. (2014) (JLA–
  B14_LAMOPEN)

- SN Ia instrinsic scatter model: Guy et al. (2010)

- SN Ia rates: Perrett et al. (2012)

- SALT2 parameter distribution: Scolnic & Kessler
  (2016) (Table 1, high-z, G10 row)

- MW dust maps: Schlafly & Finkbeiner (2011)

- Extinction law: Fitzpatrick (1999)

- Nuisance parameters: $\alpha = 0.15, \beta = 3.1$

- Cosmology: Flat ΛCDM, $\Omega_M = 0.3$, $H_0 = 70$ km s^{-1} Mpc^{-1}

The SALT2 parameters are computed using the JLA–
B14_LAMOPEN model[8], and is performed on both SMP
photometry and simulations. We show the binned red-
shift, x_1, and color distribution for the spectroscopic
sample, compared to the simulated sample, in Figure 11.
We note that the SSF used in the simulation shown here
is the one we have derived from the data; Kessler et al.
(2018) use a forward-modelling SSF, which we describe
in Section 5.3. The simulation histograms have been
normalized to the same number of SNe Ia as the spec-
troscopic sample. We use $\sqrt{N}$ errors for the observed
data, and list the χ^2/DoF for the fit between the binned
simulations and data.

There is good agreement between our simulation and
the data. The χ^2/DoF for the redshift, x_1, and color
distributions indicate agreement between the data and
simulations. This does not simply represent a judicious
choice of binning; for example, shifting the starting point
of our $\Delta c = 0.03$ bins by 0.01 in either direction leads to
χ^2/DoF< 1. We have also run a two-sided Kolmogorov-
Smirnov (KS) test using the distributions of these pa-
rameters, which for small p-values would be able to rule
out the hypothesis that the samples are drawn from the
same parent distribution. We find p-values of 0.11, 0.38,
and 0.16 for z, x_1, and c, respectively, which are consis-
tent with coming from the same distribution.

In Figure 12 we plot the two-dimensional distribution
of derived SALT2 x_1 and c from our spectroscopic sam-
ple, and compare it to a contour plot derived from a
kernel density estimator (KDE) of our simulation. In
Figure 13 we show the simulated and measured evolution
of SALT2 parameters over the redshift range of our ob-
servations. Both plots demonstrate that our data gener-
ally match the trends expected from our simulation, with
our x_1/c measurements clustered around the peak of the
KDE and an increasing (decreasing) trend with redshift
of SALT2 x_1 (c). There are some statistically signifi-
cantly differences: an overabundance of observed SNe Ia
in low-probability areas of x_1/c space, and a trend for

[8] This is an extension in wavelength coverage of the JLA–B14
model, which would otherwise only use DES-SN iz photometry in
light-curve fits of low-redshift ($z \lesssim 0.11$) SNe.

lower-than-expected x_1 values at low z. It is difficult to
state whether these differences are signs of unaccounted
bias in the spectroscopic sample selection, or rather the
intrinsic parameter model for SNe Ia in DES differs from
that determined from SDSS+PS1+SNLS data (Scolnic
& Kessler 2016).

Our SSF in Eq. (1) is clearly a simplified description
of our strategy. Supernova follow-up decisions and clas-
sification efficiency (both of which are combined into
the SSF) were functions of multiple variables beyond
peak magnitude, including host-galaxy mass, local sur-
face brightness, and observed color. We explored adding
these variables to our SSF definition, but as shown in
this Section, using just a single variable provides an ef-
fective description of the full DES-SN3YR spectroscopic
sample.

5.3. Simulation-Based Derivation

In Section 5.1 we inferred the effective selection func-
tion directly from the candidates detected in the data.
This requires making assumptions about our ability to
accurately photometrically classify SN candidates from
our full set of SSTs. While we have shown in Section 5.2
that this method succeeds in reproducing the majority
of the trends seen in our spectroscopic SN Ia sample, an
alternative approach to the SSF derivation would be a
useful check.

Using simulations without any spectroscopic selection
function, one can infer the expected magnitude distribu-
tion of real SNe Ia in our photometric data. This quantity
can then be used as the 'truth' in the denominator of the
SSF derivation. We call this approach the model-driven
selection function to differentiate from the data-driven
selection function of Section 5.1.

This method has the benefit of being insensitive to the
various uncertainties that could potentially bias our pho-
tometric classification, led by contamination from CC-
SNe. It is also highly dependent on the input model.
This includes the distribution of SN Ia SALT2 parame-
ters (x_1, c), their rate as a function of redshift, and the
intrinsic scatter model that determines the irreducible
variation in the SN Ia Hubble diagram ($\sigma_{\mathrm{intrinsic}}$). We
note that the values assumed for the SN Ia population
by Kessler et al. (2018) are commonly used, and that
extensive testing on artificial SNe inserted into images
by Kessler et al. (2018) has shown that the simulations
produce DES-like data.

In Figure 10 we show the selection functions deter-
mined using this method, with the intrinsic scatter on
the simulated SNe assumed from either the intrinsic scat-
ter models of Guy et al. (2010) (G10) or Chotard et al.
(2011) (C11). The assumption of either scatter model
results in minimal differences in the derived SSF, so for
clarity we only overplot the 1σ errors on the model as-
suming G10. The model-driven SSF efficiency ϵ is deter-
mined from a sigmoid fit to the binned data,

$$\epsilon(i_{\mathrm{peak}}) = \frac{s_0}{1 + \exp(s_1 \times i_{\mathrm{peak}} - s_2)}, \qquad (3)$$

where s_0, s_1, and s_2 are free parameters determined with
emcee (Foreman-Mackey et al. 2013). For the fitting, we
model data uncertainties using a Poisson distribution.
We perform the sigmoid fit on the data-simulation ratio
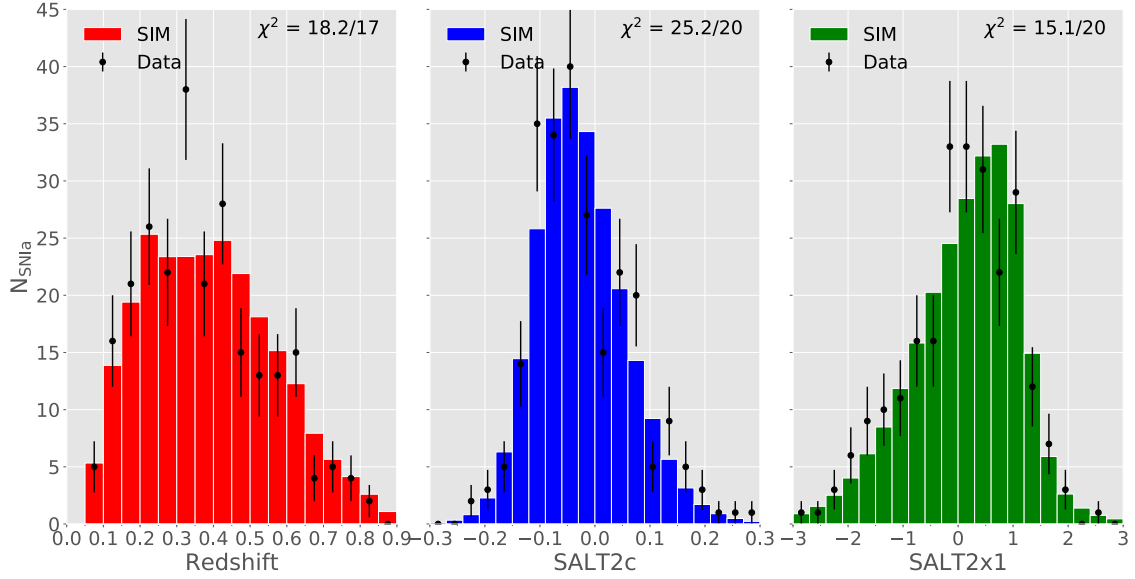
Figure 11. Distributions of redshift, SALT2 x_1, and SALT2 c for both our spectroscopic sample and a DES-like simulation using the SSF we derived from the data (and which therefore should be representative of the spectroscopic sample). The simulation is normalized to the number of points in the data histogram, and uncertainties on the data are $\sqrt{N}$ statistics. The goodness-of-fit for each histogram is shown as the χ^2 on each plot.
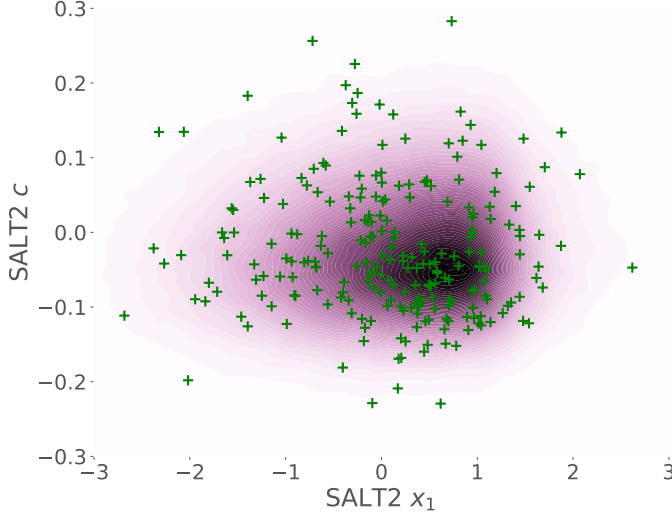
Figure 12. Joint distribution of SALT2 x_1 and c for a DES-like simulation that uses the data-driven SSF. The contours are derived from a kernal density estimator, where darker colors represent higher population density. Measured parameters from our spectroscopically confirmed SNe Ia are plotted in green.

Figure 13. Redshift evolution of SALT2 x_1 and c for a DES-like simulation that uses the data-driven SSF. The lines are rolling averages of the simulated parameters, while weighted mean and the standard deviation on the mean are shown for the data, binned by $\Delta z = 0.05$.

and then use the sigmoid amplitude, s_0, as normalization parameter. This allows the selection function to asymptote to a constant value for bright transients, go to zero for sufficiently faint transients, and transition smoothly between the two.

The two derivations of the selection function largely agree. Using the statistical uncertainties from the data-driven model and the 1σ contour from the model-based derivation, the $\chi^2/\text{DoF} = 0.7$. Visible differences between the two selection functions may be due to the assumption of a smooth sigmoid function; while classification efficiency does monotonically increase for brighter

transients on a given telescope, the strategy of having different telescopes for different targets results in a non-smoothly varying process. We run a DES-like simulation assuming this selection function, and again compare the resulting z, x_1, and c distributions to the data using the two-sample KS test. We find the probabilities that these

distributions are consistent with one another to be 0.02, 0.41, and 0.18, respectively. While the x_1 and c distributions are consistent, there is some evidence for a difference in the redshift distribution, primarily driven by an underabundance of SNe Ia in the simulation compared to data at low z. This underabundance, which peaks at $z \approx 0.25$, is similar in nature but slightly stronger than the underabundance at mid-low redshifts from the data-driven model, which peaks at $z \approx 0.35$.

We are primarily interested in the two derivations insofar as they inform our systematic uncertainty on our cosmology analysis of the spectroscopically classified sample; this is evaluated in the following section.

5.4. *Mu-Bias*

The cosmological parameter analysis and measurement of systematic uncertainties for the DES-SN3YR sample in Brout et al. (2018a) uses the model-driven SSF as a baseline. The utility of this approach is clear, as the SSF is derived from the same suite of simulations defined by Kessler et al. (2018) and used to quantify the uncertainties in the analysis. It would also be difficult to do a rigorous evaluation of systematic uncertainties owing to the photometrically-classified sample used in the data-driven approach. However, the benefit of the data-driven approach is that, being free of the assumptions that go into defining the model of the observed SNe Ia population, it allows for a cross-check of the SSF that cannot be computed from the simulations alone. Brout et al. (2018a) use a 1σ statistical fluctuation on the model-driven SSF and propagate it as a systematic uncertainty, finding the SSF to be only the ninth largest source of uncertainty in the equation-of-state parameter w.

We demonstrate the effects the SSF imparts on our observed data in Figure 14, where we show the simulated redshift-dependent bias in distance modulus for various assumptions about our selection effects. The bias ($\Delta\mu$) is computed as the difference between the distance modulus derived from fitting light curves (μ_{obs}) and the true distance modulus (μ_{true}). Each is derived from an identical simulation where the only difference is the assumed SSF. The black solid line shows the mu-bias that would be expected from a perfect spectroscopic selection; the depth of the photometry from DES means there would be nearly no bias for a perfectly selected SN Ia sample out to $z \approx 0.45$, smoothly dropping off thereafter to a bias of $\Delta\mu = 0.045$ at $z \approx 0.85$. Refer to Figure 7 for the redshift distribution of the DES-SN3YR subsample.

The data-driven and model-driven functions (shown in Figure 14 in green and red, respectively) agree on average, differing by > 0.01 mag only at the lowest and highest redshifts. The differences can be attributed to the different shapes of the selection functions (Figure 10). The steps and plateaus seen in the data-driven model are due to the binned nature of the data-driven model, while the functional form of the model-driven SSF leads to a simpler redshift evolution: flat at low z, and an effectively linear decline thereafter. The difference in mu-bias between the black line and either of the two other lines isolates the effect on the mu-bias due to the spectroscopic selection, distinct from the pipeline detection efficiency. This demonstrates that the mu-bias due explicitly to the program described in this paper lies between 0.01 to 0.03 mag over a wide range of redshift.
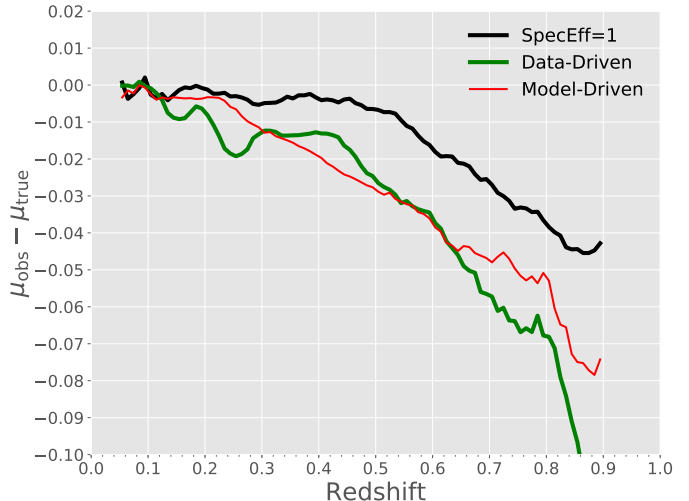
Figure 14. Redshift dependent bias derived from Spectroscopic Selection Function derivations. Black solid line shows the mu-bias derived with perfect spectroscopic efficiency, which reveals the limitations of the survey (and perfect photometric classification). The green line is the mu-bias derived from the data-driven SSF, while the red line shows the model-driven SSF. All assume an intrinsic G10 scatter model for consistency.

6. CONCLUSION

In this paper we have presented the survey operations and spectroscopic follow-up observations for the first three years of the Dark Energy Survey - Supernova Program.

We presented a detailed overview of the DES-SN observing strategy: exposure times, depths, image quality, field locations, and cadence. On average, a DES season was ~ 5.5 months long, with each of our 10 fields observed in $griz$ every 7.4 d. The median depth was ~ 23.5 mag in the eight shallow fields and ~ 24.6 mag in the two deep fields, with wider variance on a per-image basis for the bluer bands. As the best seeing typically (but not always) went to DES-wide, the median observed FWHM in $griz$ for our program was $1.41''/1.29''/1.17''/1.09''$.

We described results from our data processing pipeline, the details of which are mostly contained in other papers (Kessler et al. 2015; Goldstein et al. 2015; Gupta et al. 2016; Morganson et al. 2018). DES-SN recorded 1.21 million real single-epoch, single-filter detections—nearly 400 per image. From these detections approximately 46,000 supernova candidates were identified, which we subsequently narrowed down to 12,015 viable single-season transients. On average we discovered 24 likely supernovae per day.

We have given an overview of our live-supernova spectroscopy follow-up, consisting of Magnitude-Limited, Faint Host, Representative, and Non-Ia programs. Observations were made on an assortment of telescopes. The largest fraction by far comes from multi-object spectroscopy with the 'OzDES' on the AAT, with large allocations on VLT and Magellan and significant follow-up from Gemini, Keck, GTC, SALT, and MMT. In total we collected 1352 spectra – 1009 of which were from AAT – resulting in 251 classifications of type Ia supernovae and 56 non-Ia SNe. Our spectroscopically classified SN Ia sample spans a redshift range of $0.017 < z < 0.85$. Analyses of the SNe collected in each of these individ-

ual samples will be presented in other DES-SN papers. The host-galaxy follow-up of DES transients to obtain spectroscopic redshifts for a photometric sample – which is the primary goal of OzDES – will also be described in a future paper.

We derived the effective spectroscopic selection function (SSF) from our large, diverse follow-up program that resulted in our classified sample of DES SNe Ia. One method is data-driven, relying on photometric classification to determine the fraction of real SN Ia in our data, while the model-driven method relies on simulations of our survey. The two methods produce distinctly different shapes for our effective SSF, underscoring the different assumptions of the two models and the limitations of accurately characterizing the SSF. We show the resulting redshift-dependent bias the SSF imparts upon the measured distance modulus for each method, and remark on how this is a subdominant systematic error on the resulting cosmology analysis, as shown in the companion paper DES Collaboration (2018a).

REFERENCES

Albrecht, A., Bernstein, G., Cahn, R., et al. 2006, ArXiv e-prints, astroph/0609591
Angel, J. R. P., Hilliard, R. L., & Weymann, R. J. 1979, The MMT and the Future of Ground-Based Astronomy, 385, 87
Astier, P., Guy, J., Regnault, N., et al. 2006, A&A, 447, 31
Balland, C., Baumont, S., Basa, S., et al. 2009, A&A, 507, 85
Bernstein, J. P., Kessler, R., Kuhlmann, S., et al. 2012, ApJ, 753, 152
Bersier, D., Dennefeld, M., Smartt, S. J., et al. 2013, The Astronomer's Telegram, 5596
Betoule, M., Kessler, R., Guy, J., et al. 2014, A&A, 568, A22
Bigelow, B. C., Dressler, A. M., Shectman, S. A., & Epps, H. W. 1998, Proc. SPIE, 3355, 225

Blondin, S., & Tonry, J. L. 2007, ApJ, 666, 1024
Bronder, T. J., Hook, I. M., Astier, P., et al. 2008, A&A, 477, 717
Brout, D., Sako, M., Scolnic, D., et al. 2018, arXiv:1811.02378
Brout, D., Scolnic, D., Kessler, R., et al. 2018, arXiv:1811.02377
Burke, D. L., Rykoff, E. S., Allam, S., et al. 2018, AJ, 155, 41
Cepa, J., Aguiar-Gonzalez, M., Bland-Hawthorn, J., et al. 2003, Proc. SPIE, 4841, 1739
Childress, M. J., Lidman, C., Davis, T. M., et al. 2017, MNRAS, 472, 273
Chotard, N., Gangler, E., Aldering, G., et al. 2011, A&A, 529, L4
Conley, A., Guy, J., Sullivan, M., et al. 2011, ApJS, 192, 1
Contreras, C., Hamuy, M., Phillips, M. M., et al. 2010, AJ, 139, 519
Crawford, S. M., Still, M., Schellart, P., et al. 2010, Proc. SPIE, 7737, 773725
Croom, S., Saunders, W., & Heald, R. 2004, Anglo-Australian Observatory Epping Newsletter, 106, 12
DES Collaboration, Abbott, T., Abdalla, F. B., et al. 2016, MNRAS, 460, 1270
DES Collaboration, Abbott, T. M. C., Allam, S., et al. 2018, arXiv:1811.02374
DES Collaboration, Abbott, T. M. C., Alarcon, A., et al. 2018, arXiv:1811.02375
Diehl, H. T., Abbott, T. M. C., Annis, J., et al. 2014, Proc. SPIE, 9149, 91490V
Ellis, R. S., Sullivan, M., Nugent, P. E., et al. 2008, ApJ, 674, 51
Faber, S. M., Phillips, A. C., Kibrick, R. I., et al. 2003, Proc. SPIE, 4841, 1657
Filippenko, A. V. 1982, PASP, 94, 715
Fitzpatrick, E. L. 1999, PASP, 111, 63
Flaugher, B., Diehl, H. T., Honscheid, K., et al. 2015, AJ, 150, 150
Foley, R. J., Matheson, T., Blondin, S., et al. 2009, AJ, 137, 3731
Foley, R. J., & Kasen, D. 2011, ApJ, 729, 55
Foley, R. J., Sanders, N. E., & Kirshner, R. P. 2011, ApJ, 742, 89
Foley, R. J., Scolnic, D., Rest, A., et al. 2018, MNRAS, 475, 193
Foreman-Mackey, D., Hogg, D. W., Lang, D., & Goodman, J. 2013, PASP, 125, 306
Förster, F., Maureira, J. C., San Martín, J., et al. 2016, ApJ, 832, 155
Freudling, W., Romaniello, M., Bramich, D. M., et al. 2013, A&A, 559, A96
Frieman, J. A., Bassett, B., Becker, A., et al. 2008, AJ, 135, 338
Frohmaier, C., Sullivan, M., Nugent, P. E., Goldstein, D. A., & DeRose, J. 2017, ApJS, 230, 4
Goldstein, D. A., D'Andrea, C. B., Fischer, J. A., et al. 2015, AJ, 150, 82
Gupta, R. R., Kuhlmann, S., Kovacs, E., et al. 2016, AJ, 152, 154
Guy, J., Sullivan, M., Conley, A., et al. 2010, A&A, 523, A7
Hamuy, M., Phillips, M. M., Suntzeff, N. B., et al. 1996, AJ, 112, 2408
Hicken, M., Challis, P., Jha, S., et al. 2009, ApJ, 700, 331
Hicken, M., Challis, P., Kirshner, R. P., et al. 2012, ApJS, 200, 12
Hinton, S. R., Davis, T. M., Kim, A. G., et al. 2018, arXiv:1811.02381
Hook, I. M., Jørgensen, I., Allington-Smith, J. R., et al. 2004, PASP, 116, 425
Howell, D. A., Sullivan, M., Perrett, K., et al. 2005, ApJ, 634, 1190
Jarvis, M. J., Bonfield, D. G., Bruce, V. A., et al. 2013, MNRAS, 428, 1281
Jha, S., Kirshner, R. P., Challis, P., et al. 2006, AJ, 131, 527
Kelly, P. L., Hicken, M., Burke, D. L., Mandel, K. S., & Kirshner, R. P. 2010, ApJ, 715, 743
Kelson, D. D., Illingworth, G. D., van Dokkum, P. G., & Franx, M. 2000, ApJ, 531, 159
Kelson, D. D. 2003, PASP, 115, 688
Kessler, R., Becker, A. C., Cinabro, D., et al. 2009a, ApJS, 185, 32
Kessler, R., Bernstein, J. P., Cinabro, D., et al. 2009b, PASP, 121, 1028
Kessler, R., Marriner, J., Childress, M., et al. 2015, AJ, 150, 172
Kessler, R., Brout, D., D'Andrea, C. B., et al. 2018, arXiv:1811.02379
Kessler, R., & Scolnic, D. 2017, ApJ, 836, 56
Lampeitl, H., Smith, M., Nichol, R. C., et al. 2010, ApJ, 722, 566
Lasker, J., Kessler, R., Scolnic, D., et al. 2018, arXiv:1811.02380

Lonsdale, C. J., Smith, H. E., Rowan-Robinson, M., et al. 2003, PASP, 115, 897

Macaulay, E., Nichol, R. C., Bacon, D., et al. 2018, arXiv:1811.02376

Matheson, T., Blondin, S., Foley, R. J., et al. 2005, AJ, 129, 2352

Matsumoto, E., Shibata, T., Tominaga, N., et al. 2015, Central Bureau Electronic Telegrams, 4050, 1

Miknaitis, G., Pignata, G., Rest, A., et al. 2007, ApJ, 666, 674

Morganson, E., Gruendl, R. A., Menanteau, F., et al. 2018, PASP, 130, 74501

Narayan, G., Rest, A., Tucker, B. E., et al. 2016, The Astrophysical Journal Supplement Series, 224, 3

Neilsen, E., & Annis, J. 2014, Astronomical Data Analysis Software and Systems XXIII, 77

Oke, J. B., Cohen, J. G., Carr, M., et al. 1995, PASP, 107, 375

Pan, Y.-C., Foley, R. J., Smith, M., et al. 2017, MNRAS, 470, 4241

Papadopoulos, A., D'Andrea, C. B., Sullivan, M., et al. 2015, MNRAS, 449, 1215

Paterno, M. 2004, Calculating Efficiencies and Their Uncertainties, Tech. Rep. FERMILAB-TM-2286-CD, Fermilab

Perlmutter, S., Aldering, G., Goldhaber, G., et al. 1999, ApJ, 517, 565

Perrett, K., Sullivan, M., Conley, A., et al. 2012, AJ, 144, 59

Pierel, J. D. R., Rodney, S., Avelino, A., et al. 2018, PASP, 130, 114504

Phillips, M. M. 1993, ApJL, 413, L105

Rest, A., Scolnic, D., Foley, R. J., et al. 2014, ApJ, 795, 44

Riess, A. G., Press, W. H., & Kirshner, R. P. 1996, ApJ, 473, 88

Riess, A. G., Filippenko, A. V., Challis, P., et al. 1998, AJ, 116, 1009

Riess, A. G., Kirshner, R. P., Schmidt, B. P., et al. 1999, AJ, 117, 707

Riess, A. G., Strolger, L.-G., Tonry, J., et al. 2004, ApJ, 607, 665

Riess, A. G., Strolger, L.-G., Casertano, S., et al. 2007, ApJ, 659, 98

Riess, A. G., Rodney, S. A., Scolnic, D. M., et al. 2018, ApJ, 853, 126

Rodney, S. A., Riess, A. G., Dahlen, T., et al. 2012, ApJ, 746, 5

Sako, M., Bassett, B., Becker, A., et al. 2008, AJ, 135, 348

Sako, M., Bassett, B., Connolly, B., et al. 2011, ApJ, 738, 162

Sako, M., Bassett, B., Becker, A. C., et al. 2018, PASP, 130, 64002

Sánchez, C., Carrasco Kind, M., Lin, H., et al. 2014, MNRAS, 445, 1482

Saunders, W., Bridges, T., Gillingham, P., et al. 2004, Proc. SPIE, 5492, 389

Schlafly, E. F. & Finkbeiner, D. P. 2011, ApJ, 737, 103

Scolnic, D., Rest, A., Riess, A., et al. 2014, ApJ, 795, 45

Scolnic, D. M., Jones, D. O., Rest, A., et al. 2018, ApJ, 859, 101

Scolnic, D., & Kessler, R. 2016, ApJL, 822, L35

Shappee, B. J., Prieto, J. L., Grupe, D., et al. 2014, ApJ, 788, 48

Smith, G. A., Saunders, W., Bridges, T., et al. 2004, Proc. SPIE, 5492, 410

Smith, M. P., Nordsieck, K. H., Burgh, E. B., et al. 2006, Proc. SPIE, 6269, 62692A

Smith, M., Sullivan, M., D'Andrea, C. B., et al. 2016, ApJ, 818, L8.

Smith, M., Sullivan, M., Nichol, R. C., et al. 2018, ApJ, 854, 37.

Sullivan, M., Conley, A., Howell, D. A., et al. 2010, MNRAS, 406, 782

Sullivan, M., Guy, J., Conley, A., et al. 2011, ApJ, 737, 102

Suzuki, N., Rubin, D., Lidman, C., et al. 2012, ApJ, 746, 85

Tonry, J. L., Stubbs, C. W., Lykke, K. R., et al. 2012, ApJ, 750, 99

Tripp, R. 1998, A&A, 331, 815

Vernet, J., Dekker, H., D'Odorico, S., et al. 2011, A&A, 536, A105

Wood-Vasey, W. M., Miknaitis, G., Stubbs, C. W., et al. 2007, ApJ, 666, 694

Yuan, F., Lidman, C., Davis, T. M., et al. 2015, MNRAS, 452, 3047

Zheng, C., Romani, R. W., Sako, M., et al. 2008, AJ, 135, 1766